

Universidade Estadual Paulista “Julio de Mesquita Filho”

Programa de Pós-graduação em Ciência e Tecnologia de Materiais

Evandro Martin Lanzoni

**Electric Force Microscopy techniques on GaAs mesoscopic
structures**

Sorocaba

2018

Lanzoni, Evandro Martin.

Electric force microscopy techniques on GaAs mesoscopic structures / Evandro Martin Lanzoni, 2018
70 f.

Orientador: Elidiane Cipriano Rangel

Dissertação (Mestrado)-Universidade Estadual Paulista. Instituto de ciência e Tecnologia, Sorocaba, 2018.

1. Semicondutor. 2. KPFM. 3. AFM. I. Universidade Estadual Paulista. Instituto de ciência e Tecnologia. II. Título.

ATA DA DEFESA PÚBLICA DA DISSERTAÇÃO DE MESTRADO DE EVANDRO MARTIN LANZONI, DISCENTE DO PROGRAMA DE PÓS-GRADUAÇÃO EM CIÊNCIA E TECNOLOGIA DE MATERIAIS, DA FACULDADE DE CIÊNCIAS - CÂMPUS DE BAURU.

Aos 29 dias do mês de março do ano de 2018, às 09:30 horas, no(a) Auditório da Unesp - Campus de Sorocaba, reuniu-se a Comissão Examinadora da Defesa Pública, composta pelos seguintes membros: Prof^ª Dr^ª ELIDIANE CIPRIANO RANGEL - Orientador(a) do(a) Curso de Engenharia de Controle e Automação / ICTS/UNESP - Câmpus de Sorocaba, Prof. Dr. JOSÉ ROBERTO RIBEIRO BORTOLETO do(a) Curso de Engenharia de Controle e Automação / Instituto de Ciência e Tecnologia de Sorocaba, Prof. Dr. RICARDO PAUPITZ BARBOSA DOS SANTOS do(a) IGCE / UNESP/Rio Claro (SP), sob a presidência do primeiro, a fim de proceder a arguição pública da DISSERTAÇÃO DE MESTRADO de EVANDRO MARTIN LANZONI, intitulada **Electric Force Microscopy techniques on GaAs mesoscopic structures**. Após a exposição, o discente foi arguido oralmente pelos membros da Comissão Examinadora, tendo recebido o conceito final: aprovado. Nada mais havendo, foi lavrada a presente ata, que após lida e aprovada, foi assinada pelos membros da Comissão Examinadora.

Prof^ª Dr^ª ELIDIANE CIPRIANO RANGEL

Prof. Dr. JOSÉ ROBERTO RIBEIRO BORTOLETO



Prof. Dr. RICARDO PAUPITZ BARBOSA DOS SANTOS

Evandro Martin Lanzoni

Electric Force Microscopy techniques on GaAs mesoscopic structures

Dissertação apresentada como requisito à obtenção do título de Mestre à Universidade Estadual Paulista “Júlio de Mesquita Filho” - Programa de Pós-Graduação em Ciência e Tecnologia de Materiais, área de concentração Ciência e Engenharia de Interfaces, sob a orientação da Profa. Dra. Elidiane Cipriano Rangel e co-orientação do Prof. Dr. Christoph Friedrich Deneke

Sorocaba

2018

Agradecimentos:

Primeiramente agradeço a minha orientadora Profa. Dra. Elidiane Rangel a qual tornou possível este desafio de realizar o mestrado no programa de pós-graduação em ciência e tecnologia de materiais.

Agradeço meu ao co-orientador e líder Prof. Dr. Christoph Deneke que foi um grande guia nesta jornada, auxiliando em todo o desenvolvimento do projeto, e também em meu desenvolvimento pessoal crítico, que é fundamental para a formação de um pesquisador.

Agradeço ao Dr. Carlos Costa que foi um grande mestre e colega na microscopia de varredura por sonda. A constante troca de conhecimento que tivemos no desenrolar do projeto permitiu que os resultados fossem obtidos com total confiabilidade.

Agradeço ao Dr. Saimon Covre pelas primeiras amostras preparadas e pelas muitas discussões ao longo do projeto.

Agradeço a Ailton Garcia e Matthjin Floris pelas várias amostras cedidas.

Agradeço ao Dr. Carlos Ospina pelas imagens de HR-TEM.

Agradeço ao Dr. Suwit Kiravittaya pelo código para o cálculo numérico de uma partícula em um poço de potencial.

E por fim agradeço imensamente a toda minha família por sempre terem apoiado em minhas decisões, em especial à Mónica Arenas por ter dado apoio incondicional durante todo o decorrer do mestrado.

Dedicatória:

Dedico este trabalho ao esforço de toda minha família por acreditarem que a
educação pode transformar vidas.

Para meu pai Edilson Fernando Lanzoni (In Memoriam)

Sumário

Resumo.....	v
Abstract	vi
1. Introduction	1
2. Materials and methods.....	3
2.1. Molecular Beam Epitaxy.....	5
2.2. Mesoscopic GaAs Structures	8
2.3. Samples Investigated	11
2.4. Electron Microscopy Based techniques for pre- characterization	13
2.5. Scanning probe microscopy (SPM)	13
2.6. Kelvin probe force microscopy (KPFM).....	17
2.7. Calculation and simulation	22
3. Development and results discussion.....	28
3.1. Sample processing.....	28
3.2. Kelvin probe force microscopy measurements	31
3.3. Changing GaAs thickness	35
3.4. Changing aluminum concentration into AlGaAs barrier	36
3.5. Modelling half-finite quantum well.....	37
3.5.1. Numerical solution	37
3.5.2. KPFM of the proposed sample.....	38
3.6. Simulations of band diagram and electron wave function.....	40
3.7. Electrostatic force microscopy (EFM) without AC voltage	41
4. Conclusions	44
5. Bibliographical References	46

APPENDIX – I – Used code for particle in the box	49
APPENDIX – II – Used code for band gap and electron wavefunction	57

Resumo

As técnicas de microscopia de sonda Kelvin (KPFM) e de microscopia de força eletrostática (EFM) são amplamente utilizadas para analisar a distribuição do potencial de superfície, porém com pouca aplicação em nanoestruturas semicondutoras auto-organizadas embutidas em um substrato. Neste trabalho, investigamos diretamente o acúmulo de carga dentro de estruturas mesoscópicas de GaAs (MGS) [1]. As estruturas são fabricadas através do crescimento sobreposto de um modelo de nano orifícios usando epitaxia de feixe molecular. Para tal, uma combinação de desoxidação assistida por Ga e ataque químico por gotículas localizadas foram utilizadas para criar orifícios iniciais com uma profundidade de ca. 10 a 15nm, que são posteriormente cobertos com 15nm de barreira Al_xGa_{1-x}As e GaAs com 1nm, 2nm, 5nm, 10nm de espessura. Microscopia de força atômica e microscopia eletrônica de transmissão mostraram que a forma do orifício é preservada durante o crescimento de AlGaAs. Em seguida, esses orifícios são preenchidos com GaAs formando uma estrutura alongada sobre o buraco [1]. Investigamos o potencial de superfície local e a distribuição das cargas nestas estruturas com a técnica KPFM de passagem única. Portanto, uma voltagem AC de 5 V é aplicada a uma ponta metalizada e varremos a amostra no modo de contato intermitente. Observamos uma clara diferença de potencial na região central da estrutura, onde esperamos o furo preenchido. Então, um estudo sistemático com a técnica de KPFM mostrou a influência no acúmulo de carga quando a espessura de GaAs é alterada, bem como, quando modificamos a concentração de Al na barreira de AlGaAs. O cálculo simulando um poço de potencial com barreiras semi-finitas e finitas mostrou que não ocorre acúmulo de carga quando a espessura do GaAs é menor que 1,5 nm, corroborando com nossos resultados. Simulações do diagrama de banda e da densidade de elétron da estrutura permitem atribuir o acúmulo de carga observado, aos diferentes níveis de energia da estrutura mesoscópica de GaAs em comparação com as camadas de GaAs circundantes.

Abstract

Kelvin probe force microscopy and electric force microscopy techniques are widely used to analyze the distribution of the surface potential with little application to self-assembled semiconductor nanostructures embedded into a substrate. In this work, we directly investigate the charge accumulation inside mesoscopic GaAs structures [1]. The structures are fabricated by overgrowth of a nanohole template using molecular beam epitaxy. Therefore, a combination of Ga assisted deoxidation and local droplet etching is used to create initial holes with a depth of ca. 10 to 15nm, which are covered subsequently with 15nm of $\text{Al}_x\text{Ga}_{x-1}\text{As}$ barrier and GaAs caps with 1nm, 2nm, 5nm, 10nm thicknesses. Atomic force microscopy and transmission electron microscopy results showed that the hole shape is preserved during the AlGaAs overgrowth. Then filled with GaAs forming an elongated mound over the hole [1]. We investigate the local potential and the charge distribution in these structures with a single pass Kelvin probe force microscopy technique. Therefore, an AC voltage of 5 V is applied to a metalized tip and scanned in tapping mode over the sample. We observed a clear potential difference in Kelvin probe force microscopy measurements in the middle of the structure, where we expect a filled hole. We systematically study by Kelvin probe force microscopy the influence on the charge accumulation when the GaAs thickness is changed, as well as the Al concentration in the AlGaAs barrier. Calculation of the particle in the box for semi-finite and finite barriers were done and show that no charge accumulation is observed for GaAs thickness lower than 1.5nm in the semi-finite barrier, corroborating with our results. Simulations of band gap and electron wavefunction of the structure allow us to ascribe the charge accumulation observed, to the different confinement of carriers inside of the unstrained mesoscopic GaAs structure compared to the surrounding GaAs layers.

1. Introduction

During the last decades, development in semiconductor materials has shown an important role in our daily lives, as well as pushing many frontiers of science such as in communication, transport, power generation, medicine. The silicon based semiconductor technology has a fundamental importance in this process. Advances in smaller and more efficient transistors, diodes and all kind of semiconductor heterostructures enable to store and process data efficiently and faster in a modern cellphone than a 10 years old computer. Without the silicon based semiconductors, vacuum tubes [2] would still be the most advanced available technology and, probably, anything approaching the simplest computers available today would need an entire room.

In the same way, III – V semiconductor have gain a lot of attention due to their electronic and optical properties [1,3–5]. A particular nanostructures class of III – V semiconductor self-assemble quantum dots (QD), has been widely studied because of the potential application in lasers device and quantum computing [6,7]. In this case, the quantum dot structure combines the advantages of bulk semiconductors with those in single atom. An example is the three-dimension confinement of the structures turning the density of states in a delta-function with discrete energy emission [7,8].

In the last two decades, quantum dots fabricated using the Stranski–Krastanov growth mode gained great attention due to their potential application in opto-electronic devices [9,10]. In this process, the materials with large lattice mismatch start to grow layer by layer, but often in a critical thickness, the formation of the 3D structure is favored, producing some of the strain in the structure. Despite the advantages of the self-assemble QD, an intrinsic strain and an intermixing material during island formation is present [11,12].

To overcome the inherent strain, a new class of QDs has been investigated as an alternative to the strained self-assemble QDs. Here, materials with almost perfect match of lattice parameter, like AlGaAs and GaAs, are used to produce the strain-

free QDs. The AlGaAs/GaAs heterojunction are interesting due the well-studied optical properties when doing planar heterostructures (Quantum well and superlattice) as well as the limited intermixing at the interface make them potentially easier to model [13]. AlGaAs/GaAs QDs, cannot be obtained by Stranski-Krastanov growth mode and a different technique has to be used. One commonly used way is produce a nanohole pattern for subsequent deposition of the target material. Several approaches to prepare the hole templates, such as electron beam lithography, multistep hierarchical self-assembly, and local droplet etching, have been applied during the last years [1,4,13–15]. Da Silva *et al.* [1] combines the process of Ga-assisted deoxidation and local droplet etching to fabricate unstrained mesoscopic GaAs/AlGaAs structures (MGS). Optical characterization of this kind of structures has shown interesting properties with sharp line emission measured by micro-photoluminescence spectroscopy{Citation}.

In the recent literature, optical characterization of strain-free QDs have been well explored, works in single photon sources [16,17], tuning optical properties by external strain [18–20] and optical control of the nuclear spin for potential application in quantum computing [3,21,22] are examples found in the literature. Until now, there is no electrical characterization of strain-free QDs at the nanoscale.

In this work, we used Kelvin probe force microscopy (KPFM) to directly probe the electrostatic properties of the mesoscopic GaAs Structure (MGS) proposed by da Silva *et al.* KPFM technique provides quantitative information of the sample surface potential with lateral resolution around 25nm. The main advantage of this technique is measuring quantitatively the difference surface potential with 15 mV resolution without current between tip and sample.

Finally, we carried out the KPFM measurement, which shows a difference surface potential in the middle of the MGS samples, where we would expect the initial hole. Increasing the thickness of the GaAs cap and changing the AlGaAs content, we observed changes in the difference surface potential. A numeral simulation of the half-infinite quantum well -band diagram and the electron wave function, assist us a better understanding of that, for GaAs thickness lower than 1.2nm there is no confinement, in accordance to our experimental results.

2. Materials and methods

Figure 2.1 shows a schematic example of size confinement and its consequence for the energy level. In a bulk structure, the states of energy are closely spaced that the energy appear as a continuously increasing function. Reducing the material in one axis (2D – Quantum well, 1D – Quantum wire) the energy is quantized. When the material is reduced in the three dimensions (0D – Quantum dot), the carriers or electrons inside the material start to confine, and the structure assumes properties of a single atom, like the discrete quantized energies.

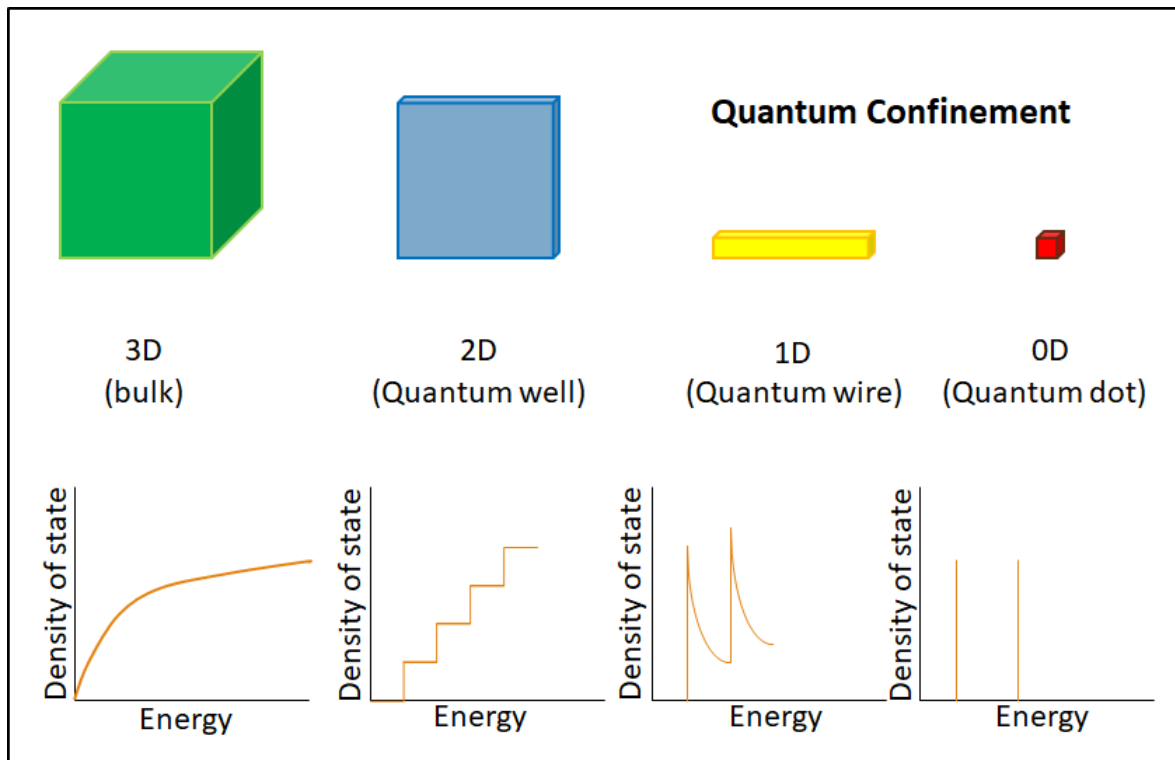


Figure 2.1: Schematic of size reduction for a quantum confinement. The 3D material (bulk) have continuous density of states in function of the energy. When reducing the size in the x (quantum well), y (quantum wire) and z (quantum dot) directions the energy starts to be quantized.

One way for size confinement is preparing two different semiconductors in contact to each other, doing a heterojunction. The combination of multiple heterojunction give rise to the heterostructures, which in the year 2000, Herbert

Kroemer and Zhores I. Alferov were awarded with the Nobel Prize in Physics for “developing semiconductor heterostructures in high-speed and opto-electronic devices”.

devices”.

In order to obtain good optical and electrical properties, it is essential that interface between the semiconductors is free of dislocations or defects. With the advances of molecular beam epitaxy (MBE) and the vacuum chemical deposition (CVD) high quality heterojunction or heterostructures start to improve the performance of semiconductor devices [23–26].

The Figure 2.2 (a) illustrates a typical example of a heterostructure combining two different semiconductors that allow continuous transition of carriers through the interfaces of the two materials. The band gap difference between the semiconductors produce the carrier confinement effect. The Figure 2.2 (b) shows the simulation by NextNano of a quantum well using GaAs sandwiched between two $\text{Al}_{0,3}\text{Ga}_{0,7}\text{As}$ barriers. The following figure show the conduction band edges and the lowest confined eigenstates for 6nm of AlGaAs/GaAs quantum well.

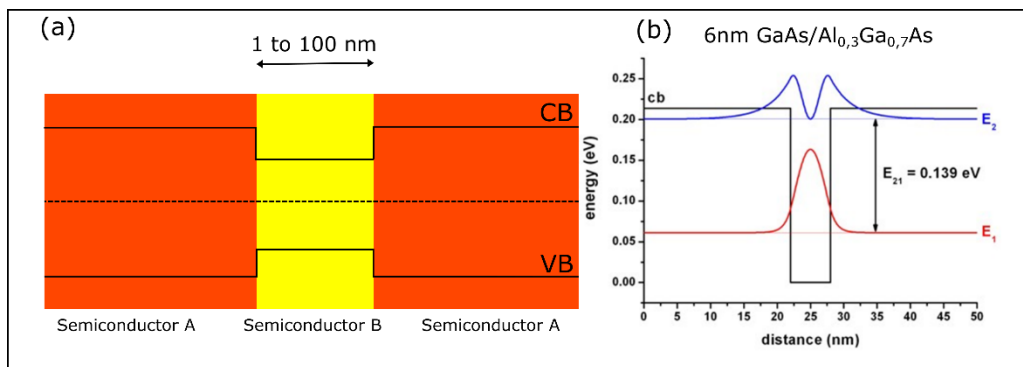


Figure 2.2: (a) General semiconductor interface for carrier confinement. The different bandgap between the semiconductor A and B create a potential well. (b) NextNano simulation for a quantum well using 6nm of GaAs sandwiched with AlGaAs.

2.1. Molecular Beam Epitaxy

Molecular Beam Epitaxy (MBE) is widely used in the manufacturing of semiconductor devices, and is considered one of the fundamental tools for the development of the nanotechnology. In the last decades, MBE has made some impressive contributions to fundamental studies of the growth of low dimensional structures and to basic concepts of thin film growth, as well as to surface studies in general [6,27].

MBE is a versatile ultrahigh vacuum technique for growing multiple epitaxial layers of semiconductor crystals with high precision. The extreme control of the MBE technique over composition variation, interface sharpness, impurity doping profiles, and epitaxial layer thickness to the atomic level makes it possible to demonstrate a wide variety of novel semiconductor structures [14,28]. Since its invention, nearly 40 years ago, the MBE technique has evolved from a laboratory apparatus for exploring new materials and novel devices to a favored tool for the mass production of III–V high-speed devices.

In the MBE process, beams of atoms are incident upon a heated crystal atomically clean in an ultra-high vacuum environment. The arriving atoms form a crystalline layer following the lattice parameter of the substrate (Figure 2.3). Thus, it is possible to produce unique structures precisely controlled in composition. Examples of structures grown by MBE, include quantum well devices, superlattices and lasers.

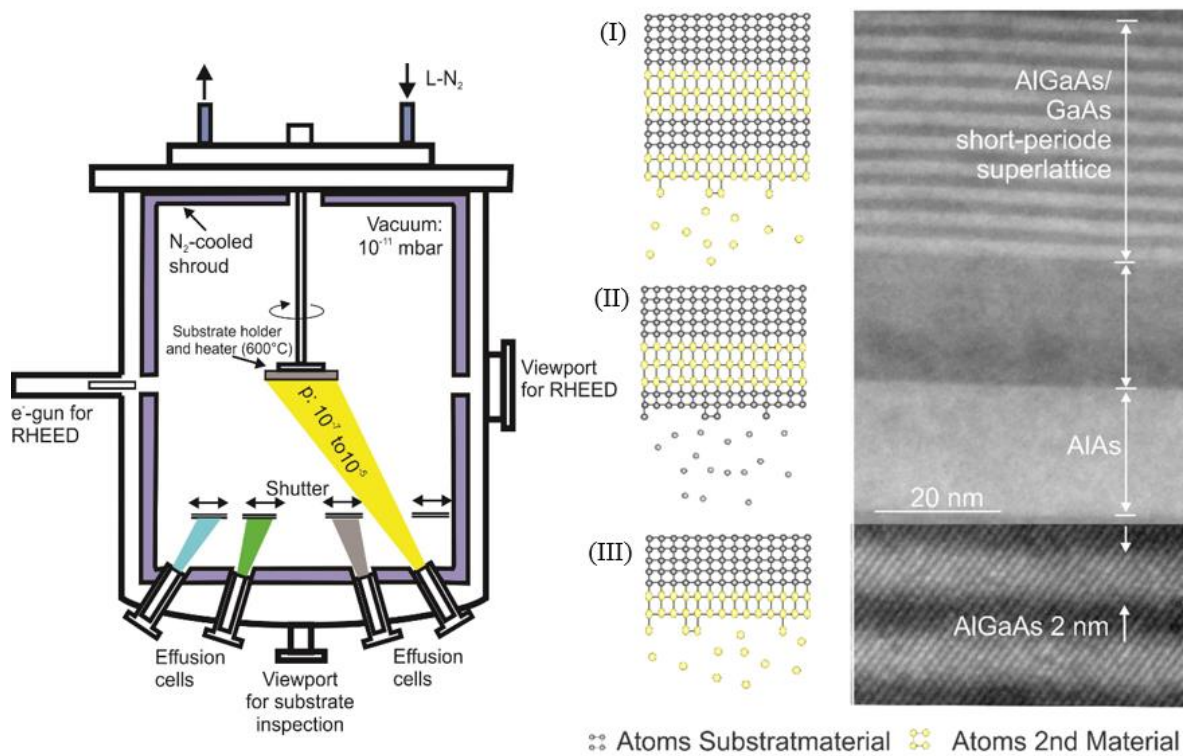


Figure 2.3: Schematic of molecular beam epitaxy deposition. Inside the UHV chamber the interest material is evaporate in a controlled tax, and following the lattice parameter of the substrate. Is possible change the material during the growth and obtain a heterostructure like showed in TEM image (right side).

In Figure 2.3 a schematic model for molecular beam epitaxy (MBE) is shown. The substrate is mounted on a heater plate inside the main UHV chamber. Different materials can be evaporated together or individually while a reflection high energy electron diffraction (RHEED) system provides a diffraction pattern on a phosphor-coated window allowing in-situ monitor the ordering of the substrate surface. Therefore, layer by layer of the interest material grow following the lattice parameter of the substrate, as shown in Figure 2.3 (I, II and III). In this schematic model four effusion cells are placed at the main UHV chamber. In the currently MBE system that we used to prepare the sample the four effusion cells were Arsenic, Aluminum, Gallium, Indium (Figure 2.4)

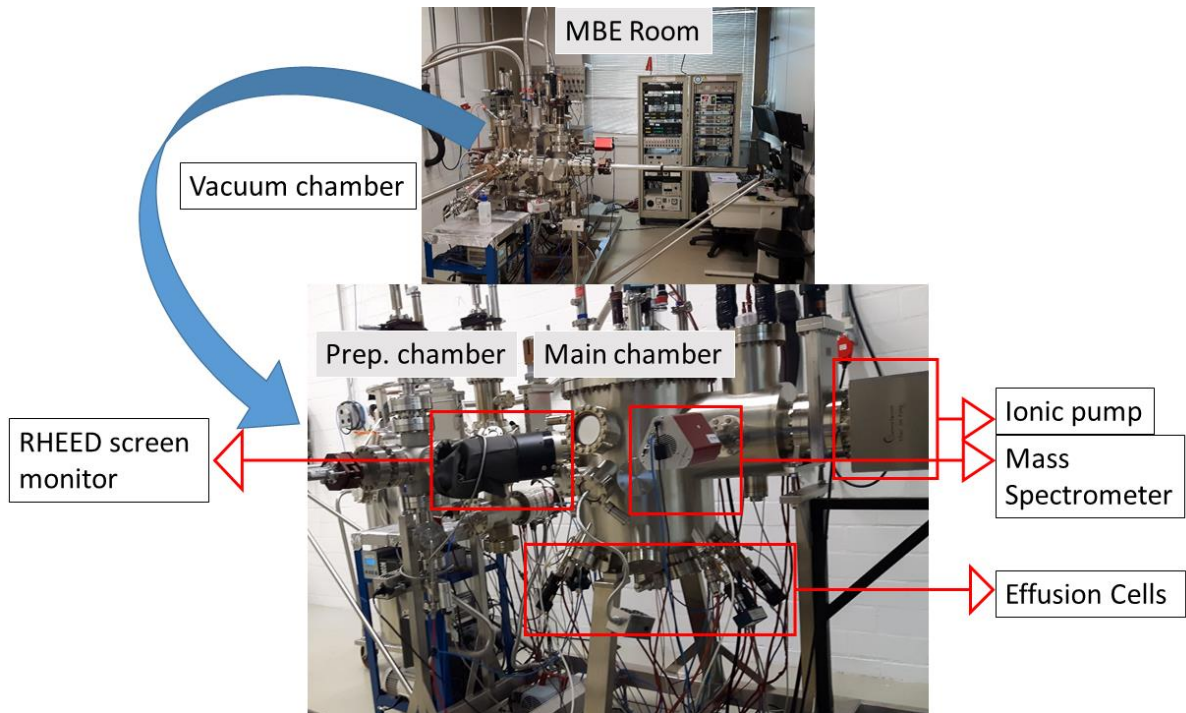


Figure 2.4: Molecular Beam epitaxy system used in this project. Introduction, preparation and main chambers compose the vacuum system. The sample is grown in the main chamber, where four effusion cells (As, Ga, Al, In) and two doping cells (Si, Be) is used for material deposition, and monitored by reflection high energy electron diffraction (RHEED).

Figure 2.4 shows the molecular beam epitaxy system used in this project. The machine is localized at Brazilian Nanotechnology National Laboratory – LNNano and is able to growth epitaxial thin film with the III – V elements of the periodic table. The current setup has four effusion cells (Ga, As, In, Al) and two doping cells (Si and Be). In Figure 2.4 is possible to identify some of the main components of the MBE among which, the main chamber with effusion cells, preparation chamber, introduction chamber, mechanical and ionic pump, RHEED screen monitor, cooling system and mass spectrometer.

2.2. Mesoscopic GaAs Structures

Recently, there has been a development of unstrained quantum dots [29]. In this process, materials with similar lattice parameter but different band gap are used to produce the quantum dots.

To prepare the mesoscopic structures, normally first a hole template is created and then is deposited the material of interest. There are two different ways to prepare the pattern of holes, the ex-situ and the in-situ procedures (Figure 2.5). In the ex-situ process, an external technique, such as electron beam lithography, is used to locally etch the sample producing the holes. Precise and uniform holes are prepared by using this process, but the disadvantage of the ex-situ procedure, is that the sample preparation is not completely carry out inside the UHV chamber of the MBE. On the other hand, in the in-situ procedure, the entire process is carry out inside the UHV chamber of the MBE avoiding the disadvantage of the ex-situ patterning.

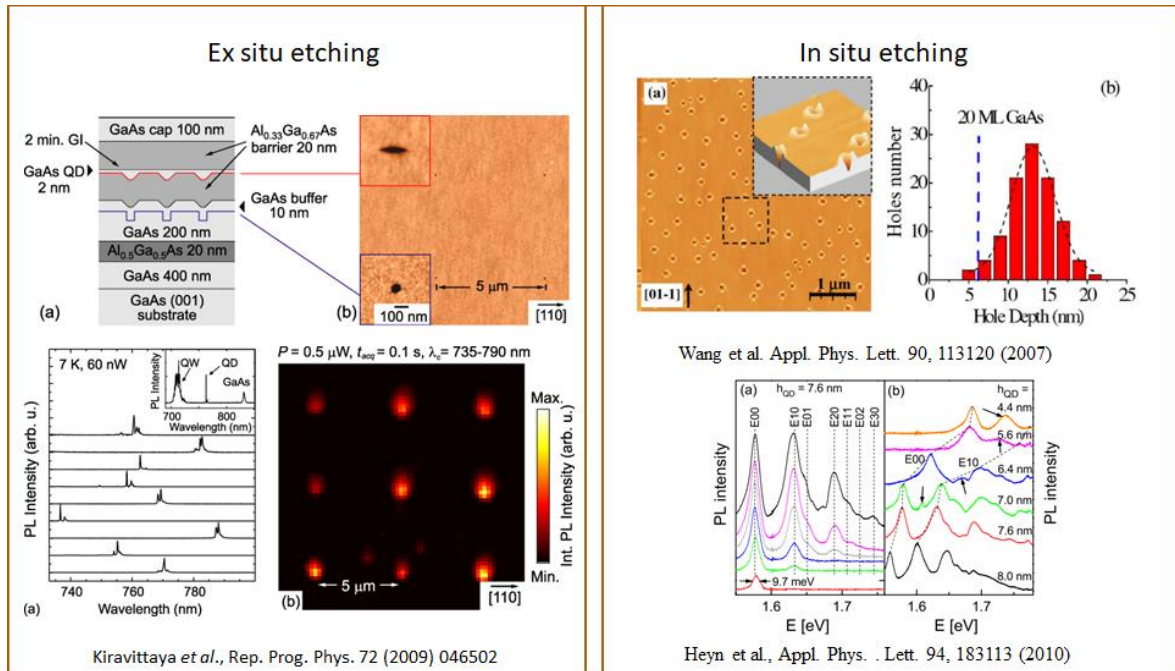


Figure 2.5: Examples from the literature of ex-situ and in-situ etching process for the holes template. In the left side, the ex-situ process used by Kiravittaya et.al. which used the electron beam lithography to produce the patterns. In the right side, local droplet etching was employed

by Wang et.al. and Heyn et.al. in an in-situ procedure. In both procedures were observed photoluminescence intensity due to the unstrained QD.

In this project, we used the in-situ procedure combining two methods for the etching process: the gallium assisted deoxidation and a nanodrill technique called local droplet etching (LDE). During the gallium assisted deoxidation, the native oxide is removed using a higher pressure of gallium to reduce the stable gallium oxide, which occurs by the reaction $\text{Ga}_2\text{O}_3 + 4\text{Ga} \rightarrow 3\text{Ga}_2\text{O}$ [30–33]. This leads to a flat, and oxide-free surface that has been successfully used to patterned substrates with features several microns wide [15,30]. After removing the native oxide from the sample surface the local droplet etching is used to prepare the hole template. The fabrication of such nanoholes was first demonstrated by Wang et. al. [15] on GaAs surfaces using gallium as etchant. The LDE technique is related to the droplet epitaxy where Ga droplets are formed on crystalline surfaces in a Volmer–Weber–type growth mode, which in a subsequent step were crystallized under As pressure [1,4,14,15,29]. During this process, the higher concentration of Gallium starts to react with GaAs substrate generating holes with controllable 3 dimension size. Creation of a variety of semiconductor nanostructures such as quantum dots, quantum rings and double rings has already been demonstrated [14,29,34,35]. The Figure 2.6 ((I) a, b and c) show a schematic procedure of Gallium assisted deoxidation and the Figure 2.6 ((I) d, e and f) show the LDE technique.

Using the hole template, the material deposition starts for the unstrained quantum dots. At first step, 15nm of AlGaAs is grown over the GaAs substrate. Then different thickness of GaAs is used to filled the structure. AlGaAs and GaAs have similar lattice parameter ($\sim 5.653 \text{ \AA}$) and grow epitaxially without strain. However, the main advantage of this system is because changing the Al concentration of the AlGaAs barrier, the band gap can be tuned from 1.42 eV (GaAs) to 2.16 eV (AlAs) [36]. Thus, samples with different Al concentration was produced. The MGS structures have one more barrier of AlGaAs and GaAs cap layer to protect the system. However, to access the internal region of the sample these two final steps were not carry out.

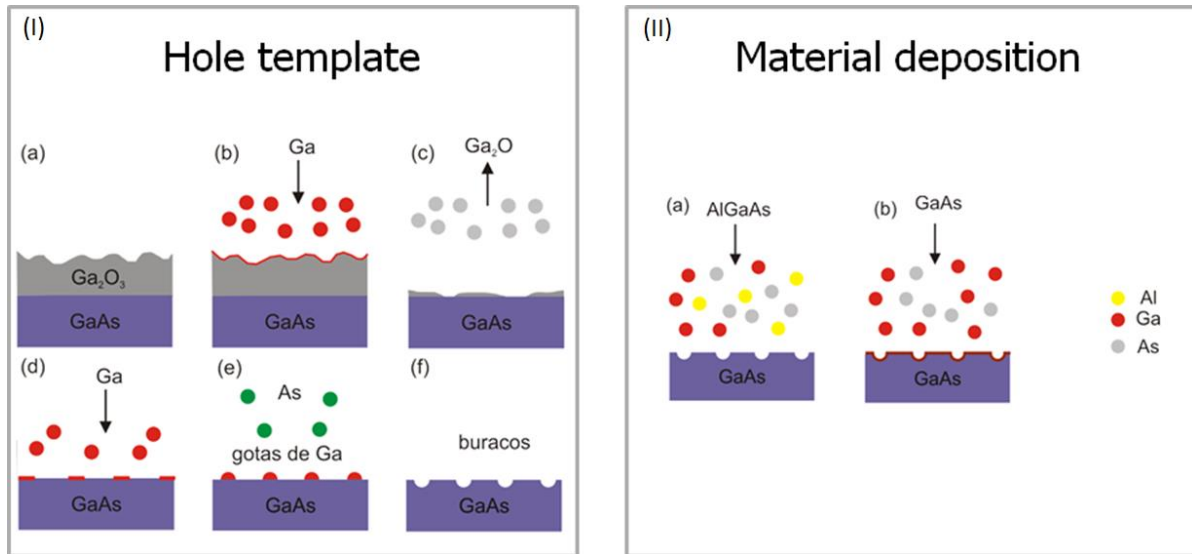


Figure 2.6: Gallium assisted deoxidation, Local droplet etching and material deposition procedures. High concentration of Ga removed the native oxide layer and then with As atmosphere starts to nanodrill the GaAs substrate producing a hole template. AlGaAs and GaAs is grown to produce the unstrained quantum dots. Adapted figure from Saimon C. da Silva thesis.

Part of the structures analyzed in this work were previously studied by da Silva *et al.* [1] where is demonstrated a good controllability over size and morphology by changing growth parameters, as well as interesting optical properties. Figure 2.7a shows μ -photoluminescence (μ -PL) spectra maps obtained at 10K. From this map is possible to clearly identify three different contributions. At 1.88eV a strong signal comes from the quantum well formed by the material surrounding the MGS structure. Structures with thickness smaller than 15nm is emitting in the energy range between 1.58 and 1.72eV, and the deep holes (15 to 19nm thickness) is emitting at 1.54eV. In the Figure 2.7b, μ -PL is carried out on a single structure. A sharp line emission is identified with linewidth of the peak ca. 370 μ eV.

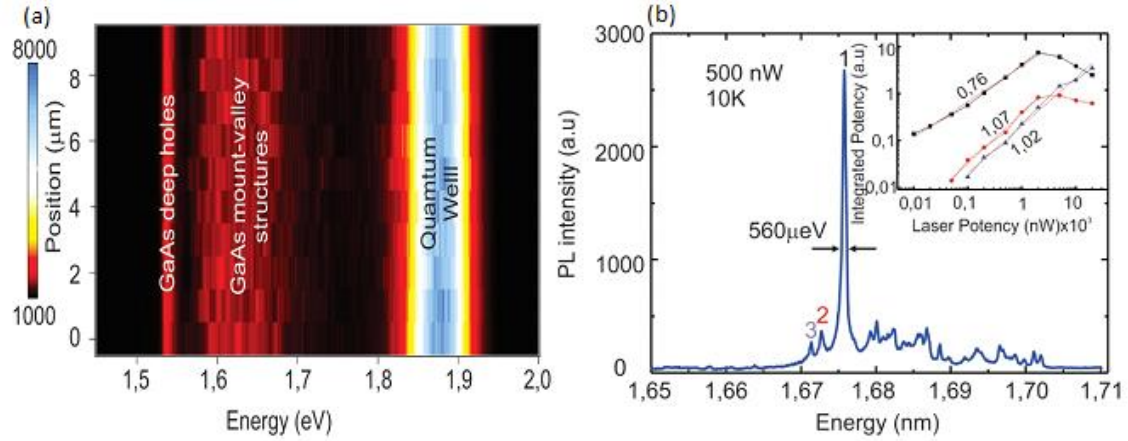


Figure 2.7: (a) μ -Photoluminescence intensity map with a large spot size ($5 \mu\text{m}$). (b) μ -Photoluminescence spectrum of a single MGS showing a sharp line emission with high potentiality for optical applications.

2.3. Samples Investigated

Using the described methods, we prepare the set of sample shown in **Table 1**. We measure the entire set of sample from this table. The sample P323 is only the substrate with the hole templates made by LDE. Sample P325 is the hole template covered is the AlGaAs barrier. Then, two sets of sample was prepared. In the first set (P144, P149, P152 and P155) aluminum barrier was grown with 33% Aluminum content and filled with different thickness of GaAs. In the second set of samples (P325, P326, P327, P328), we change de Aluminum content of the AlGaAs barrier. Finally, the process of cooling down the sample was changed in the way that the GaAs layer follow the shape of the hole template. With this procedure 1nm (P359) and 2nm (P369) thickness of GaAs was grown.

Table 1. Table with the measured samples names and showing the changed parameters for each experiment. Five different set of sample were prepared: Only hole template, holes filled with AlGaAs barrier, holes with AlGaAs barrier and changing the thickness of the GaAs, changing the concentration of the AlGaAs barrier and AlGaAs/GaAs following the hole shape of the structures.

		Grown structures			
		Only holes			
GaAs holes		P323			
		AlGaAs Barrier			
AlGaAs Barrier GaAs holes		P325			
		Changing GaAs thickness			
		Thickness			
		1nm	2nm	5nm	10nm
GaAs AlGaAs Barrier GaAs holes		P155	P152	P144	P149
		Changing AlGaAs concentration			
		Al content			
		33%	50%	70%	90%
AlGaAs Barrier GaAs holes		P325	P326	P327	P328
		GaAs Following the hole shape (Particle in the box)			
		GaAs thickness			
		1nm		2nm	
GaAs AlGaAs Barrier GaAs holes		P359		P369	

2.4. Electron Microscopy Based techniques for pre-characterization

For pre-characterization of our samples, electron microscopy based technique was employed. The High-resolution transmission electron microscopy (HR-TEM) is a powerful technique that provides an image with the atomic structure of the sample. To check dislocations and defects, that could be prejudicial to the optical and electronic quality of the sample, we used the double correct transmission electron microscope TITAN Themis Cubed – FEI. The sample preparation for HR-TEM was done in the Helios NanoLab DualBeam – FEI. This equipment combines the scanning electron microscopy (SEM) with the focus ion beam (FIB) for nanomanipulation of the sample. With FIB, a cross-section cut was done right on the middle of the structure to observe the AlGaAs/GaAs heterojunction. Both equipment are located at Brazilian Nanotechnology National Laboratory – LNNano/CNPEN.

2.5. Scanning probe microscopy (SPM)

Scanning probe microscopy (SPM) is a group of versatile techniques to imaging sample surface in three dimensions. The beginning of SPM comes from 1981 when Binnig et.al. observed for the first time tunneling through a controllable vacuum gap given rise to scanning tunneling microscopy (STM) [37]. The main idea of this experiment was use a tungsten (W) sharp tip connected to a piezoelectric material and measure the spectroscopy tunneling current when approaching to a Pt substrate. In 1982 the same authors combined the tunneling effect with the precise movement of piezoelectric material. STM with atomic spatial resolution was now tried out on surfaces of CaIrSn₄ and Au samples in vacuum atmosphere [38]. This experiment awarded Binnig and Rohrer with the Nobel Prize in physics in 1986.

The STM was the first powerful scanning probe microscopy technique invented, but this technique is limited to conductive material and need some special sample preparation for ultra-high vacuum. In 1985, using the principle of the STM

to control forces around $10^{-18}N$ in air, Binnig and Quate propose the atomic force microscopy (AFM) to measure insulators with atomic resolution [39]. This experiment open experiment open a range of new sophisticated techniques based on scanning probe microscopy. Nowadays, SPM has more than 30 different techniques commercially available with especial emphasis to topographical modes (AFM, STM, phase contrast, etc.), electrical modes (EFM, KPFM, SCM, etc.) [40–43] and magnetic mode (MFM) [44,45].

The basic principle of the SPM is measure the different kind of interactions (e.g. Van der Waals force, Coulomb force, magnetic force, tunneling) between tip and sample (Figure 2.8). A high precise system to analyze and process the interaction signal is used to build a 3D image.

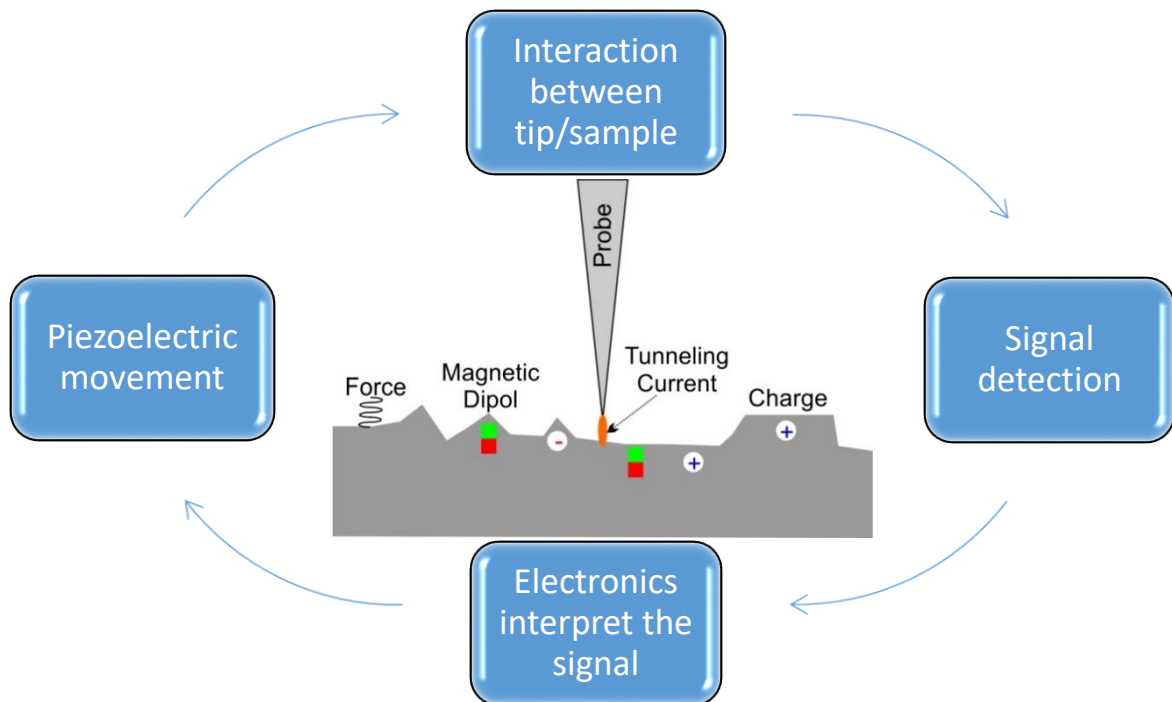


Figure 2.8: Basic principle of scanning probe microscopy (SPM). A sensitive system is used to detect different kind of interaction between tip and sample. The result signal is interpreted to build a 3D map.

The most known SPM technique is the atomic force microscopy (AFM). Here, a sharp tip is located in the edge of a silicon cantilever and placed close or sometimes in contact with the sample to scan the surface. The basic principle of the AFM is detect the

involved forces (Pauli interaction and van der Waals) in the Lennard-Jones potential between tip and sample (Figure 2.9). The AFM is based on a laser movement in a photodetector when different gradient forces act to the tip. Therefore, the laser is focused on the top side of the cantilever and the reflection light is monitored using a four-quadrant photodetector. There are three different modes to operate the AFM that are dependent on the distance d between tip and sample: contact (red square in Figure 2.9), intermittent contact and non-contact mode (blue square in Figure 2.9). In the first one, the tip is located a few nanometer to the sample (in contact) where the Pauli interaction is the main responsible to exert forces between tip and sample. The generated force will deflect the tip changing the laser signal in the photodetector, and then the piezoelectric material correct the position of the tip to build a 3D topographical image. In intermittent contact mode, the tip oscillate at the resonance frequency of the cantilever. To build an image, the microscope try to keep a constant oscillation amplitude of the tip. When the tip pass over a sample step the amplitude change and immediately the electronic system of the microscope correct the height with the piezoelectric material. The non-contact mode works similar to tapping mode, the difference is the oscillation amplitude. As the range of van der Waals interaction is not higher than 10nm, in non-contact mode the oscillation amplitude cannot be higher than 10nm. In this way, non-contact mode use smaller values for oscillation amplitude compare to intermittent contact mode, and is recommended only for flat surface. Regardless the used mode, the AFM technique provide the topographical information with high resolution in 3D axis.

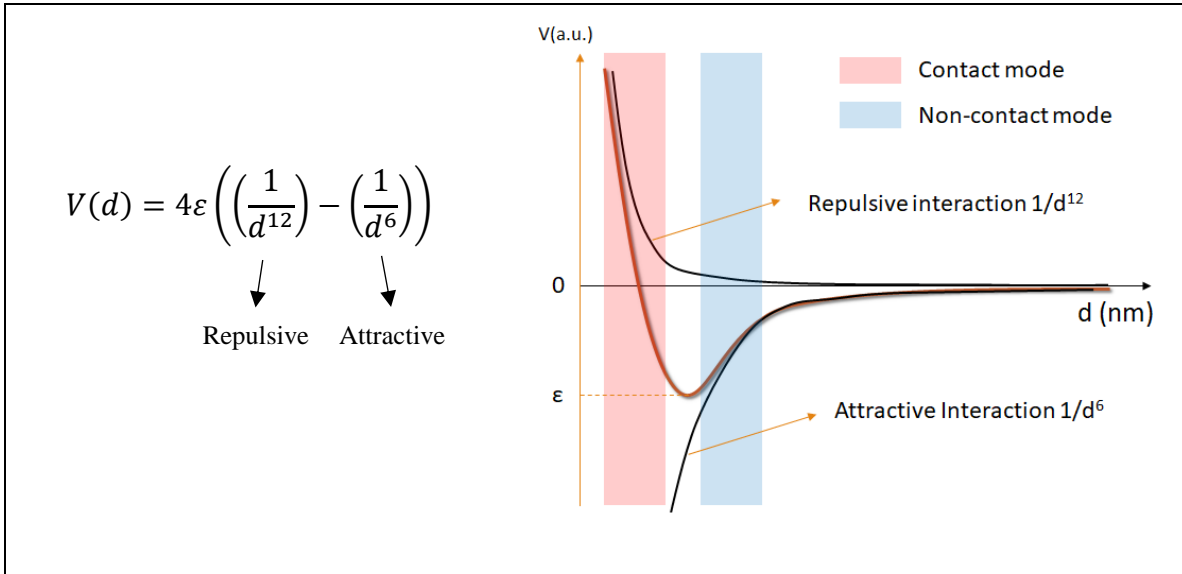


Figure 2.9: Lennard-Jones potential for the AFM techniques. Repulsive interaction or Pauli interaction, proportional to $1/d^{12}$, used in contact mode. Attractive interaction or van der Waals force, proportional to $1/d^6$, used in non-contact mode.

Because of the powerful and high precise tool to acquire topographical information, the SPM is an excellent technique to probe long-range forces such as magnetic forces and electrostatic forces. As showed in Figure 2.9, van der Waals and Pauli interaction between tip and sample are used to acquire the topographical information. But, as the long range forces are much more stronger at long distances (longer than 10nm), the SPM can be applied to measure long-range forces keeping a constant distance to the sample surface. Therefore, the van der Waals interaction is insignificant compared to the long range force as demonstrated in Figure 2.10 by Saint Jean *et al* [46]. Assuming the tip geometry as a sphere-cone model and sample surface as a plane, Saint Jean demonstrated that in long distance the predominant force through the tip is due the long-range forces. In this way, the SPM can be applied to simultaneously acquire topographic image when tip is close to the sample surface, and in a second pass, the electrostatic information keeping a constant distance between tip and sample. This technique is called electrostatic force microscopy (EFM).

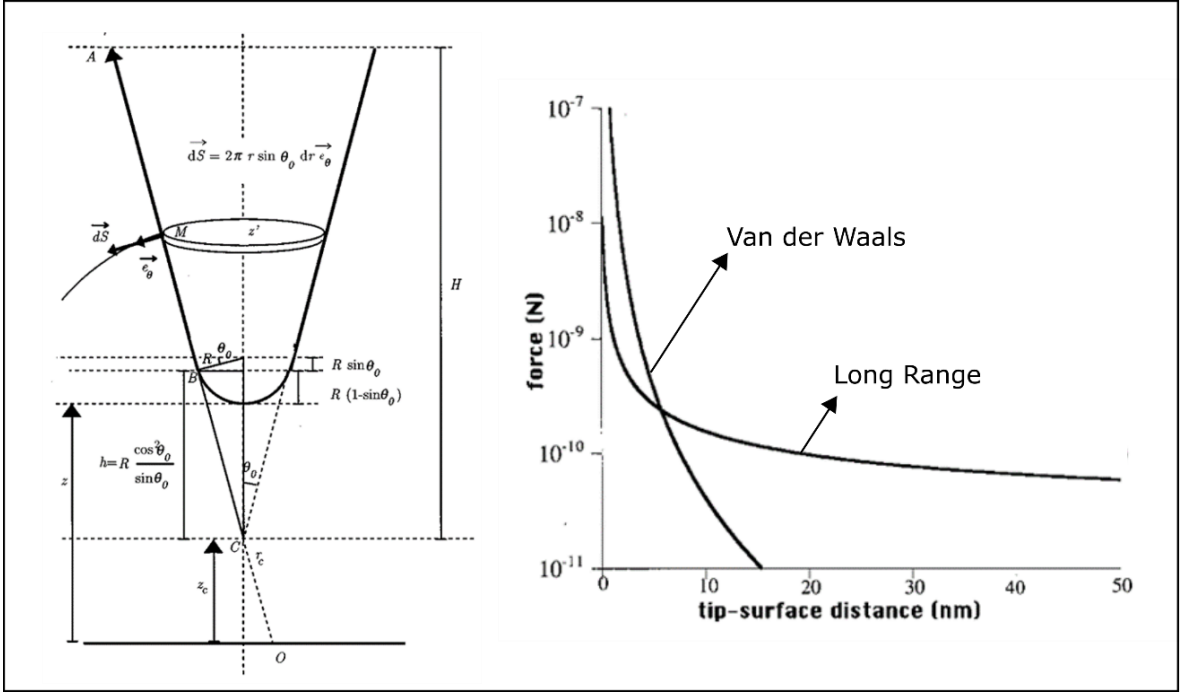


Figure 2.10: Adapted figure from Saint Jean *et al.* [46] simulating a comparison between van der Waals interaction and long-range forces. Saint Jean *et al.* described the tip as a sphere-cone model whereas the sample surface is supposed to be plane (left side). The long-range curve start to be stronger than van der Waals when distance between tip and sample is higher than ~ 8 nm.

Over the years, enhanced EFM techniques have been explored such as Kelvin probe force microscopy (KPFM). In this work, we are interested to quantitatively direct probe electrostatic forces over the sample surface of strain-free QDs. Therefore, KPFM will be employed.

2.6. Kelvin probe force microscopy (KPFM)

After development of the atomic force microscopy (AFM) that essentially measure the involved forces in the Lennard-Jones potential, researchers start to explore the different forces acting between tip and sample. In 1988 Stern *et al.* [40] detected charges on polymethylmethacrylate and single crystal of sapphire. This was the first time that electrostatic charges were detected using SPM, later called electrostatic force microscopy (EFM).

EFM use a silicon tip covered with Pt/Ir to measure in double pass topography and electrostatic forces of the sample surface. In the first pass, the microscope monitor the amplitude vibration of the tip in intermittent contact mode to acquire the topography of the sample. In the second pass, the tip is lifted tens of nm and follow the topographical profile keeping constant height between tip and sample. At this distance, the long-range forces are predominant over the van der Waals interaction as showed in the Chapter 2.5. Therefore, each time the tip pass over electrostatic charge an electric field act between tip and sample generating an acting force. This force deflect the cantilever, changing amplitude and phase signals of the tip oscillation. Using a lock-in amplifier is possible to qualitatively acquire the electrostatic forces acting to the tip. Thereby, EFM is a powerful and well-established technique to qualitative detect electrostatic forces with high lateral resolution.

In 1991 Nonnenmacher *et.al.* used the principle of the parallel plate capacitor proposed in the late 19th century by Lord Kelvin and combined it with SPM to quantitative measure the electrostatic force over the sample surface with nanometer lateral scale [42]. In the Lord Kelvin method, two conducting materials are arranged as a parallel plate capacitor with a small spacing in between. In a simple model, the contact potential between the two materials is $V_{CPD} = \frac{1}{e}(\phi_1 - \phi_2)$, where ϕ_1 and ϕ_2 are the work function of the conductors including changes due to absorption layer on the surface. A periodic vibration of the distance between two plates at ω frequency results in a current $i(t)$ given by

$$i(t) = V_{CPD}\omega\Delta C \cos \omega t, \quad (1)$$

where ΔC is the change in capacitance. For the actual measure of V_{CPD} , an additional bucking voltage is applied between the two plates until the space in between is filed free and the current $i(t)$ goes to zero.

In the KPFM technique, the acting force between tip and sample will be measured instead the current. Allied to this, an additional DC voltage is applied between tip and sample until the gradient force in between minimizes. Therefore, KPFM technique uses the fact of tip and sample build a parallel plate capacitor when close to each other, and the electrostatic force F can be written as:

$$F = -\frac{1}{2} \frac{dC}{dz} V^2 \quad (2)$$

where C is the tip to sample capacitance.

We assume that the voltage V is composed of the contact potential V_{CPD} plus applied DC and AC voltages (V_{DC} and V_{AC} respectively). Then, the electric force can be written as the following equations:

$$F = -\frac{1}{2} \frac{dC}{dz} [(V_{DC} + V_{CPD} + V_{AC})^2] \quad (3)$$

The main advantage of KPFM comes from the fact that, topographical and quantitative electrostatic surface charge maps are obtained simultaneously in a single pass. The Figure 2.11 shows a schematic diagram of the KPFM method. A silicon tip covered with Pt/Ir is oscillated at its mechanical resonance frequency (ω_m). The *lock-in amplifier I* will analyse the deflection signal of the tip at ω_m frequency in order to the *Z Servo* build the topography image. Simultaneously an AC voltage with frequency ω_e is applied between tip and sample. When the local electric field is changing, the amplitude and phase of the AC signal will change too. At this point, *lock-in amplifier II* set at ω_e frequency read phase and amplitude oscillation. Subsequently the *KPFM Servo* applied a DC voltage in order to minimize the mechanical oscillation at ω_e frequency. When *lock-in amplifier II* identifies no mechanical oscillation, the DC tip voltage will be the same as the unknown surface potential. Then the DC signal is recorded by the software, and used to build the electrostatic surface potential maps.

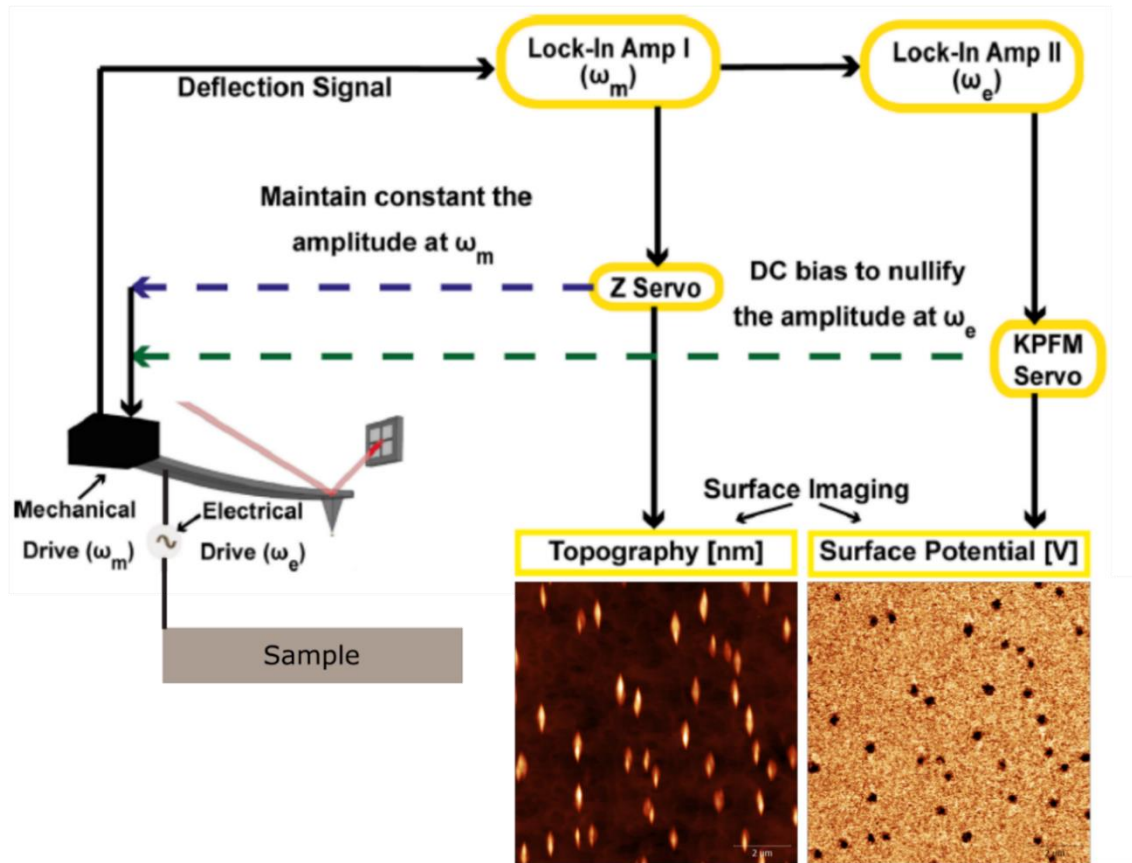


Figure 2.11: Schematic diagram of the KPFM method. In single pass measurements, Topography and surface potential is acquired simultaneously. The “lock-in amplifier I” analyses the cantilever deflection at resonance frequency of the tip and try to keep constant oscillation amplitude to acquire topography image. At the same time, the lock-in amplifier II analyses the AC frequency and use a servo to apply DC bias nullifying tip oscillation at AC frequency [47] (Adapted image).

The KPFM is a well establish technique and has been used as an important tool at the semiconductor world [48]. In the literature is possible to find a great variety of works using the KPFM [48–51], but this kind of characterization has not yet applied to directly probe the charge accumulation inside unstrained quantum dots.

Kelvin probe force microscopy (KPFM) technique was used to measure the surface potential of the samples. The KPFM acquires in a single pass the topography and the surface potential simultaneously. In intermittent contact mode, the mechanical oscillation of the tip is tracked by the photodetector and analyzed by two feedback loops. The first loop is used in the conventional way to control the distance between tip and sample surface, while

scanning the sample at constant oscillation amplitude. The second loop is used to minimize the electric field between tip and sample by adjusting the DC tip bias voltage to minimize electrostatic forces between tip and sample. In this way, an AC signal is applied to the tip at 13 kHz or 17 kHz (depending the tip used). A second lock-in amplifier is monitoring the AC frequency, so that for each point, a DC bias is added to the tip to nullify any oscillation caused by electrostatic forces.

In this project we used the following scanning probe microscopy: NX-10 – Park Systems, FlexAFM – Nanosurf and NanoIR2-s – Anasys Instruments operated in EFM-based techniques using PPP-EFM – Nanosensors tips. The entire images were treated using the Gwyddion software correlating topography and electrostatic potential data at the same position. Almost all the samples presented an average surface potential around 0.6 V that we normalized for all the measurement, in order to get a comparable scale between 0 and 100 mV. This procedure does not interfere with the project conclusion since we are not interested in the quantitative value for the surface potential. We are looking only for the difference potential between the structures and the surrounding surface.

2.7. Calculation and simulation

For the mathematical understanding of our sample, we use the fact of the different band gap in the GaAs/AlGaAs heterojunction generated a well-known problem of a particle in the box with half-infinite potential barrier Figure 2.12.

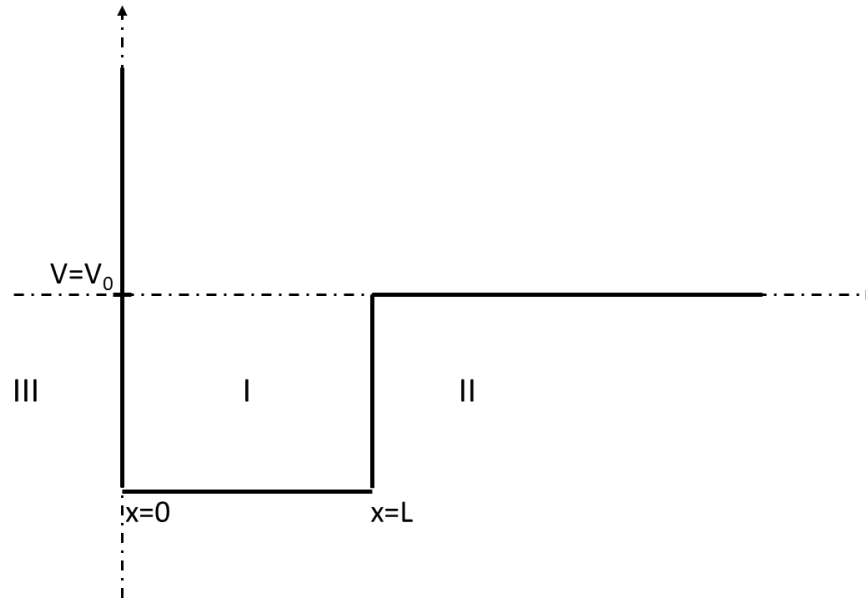


Figure 2.12: Potential energy for a particle in a half-infinite box in one dimension.

In this case, the potential energy is given by

$$V(x) = \begin{cases} \infty, & x < 0 \\ 0, & 0 \leq x \leq L \\ V_0, & x > L \end{cases} \quad (4)$$

Solving the Schrodinger equation for the region I, II and III:

Region III solution

The Schrödinger equation in region III is

$$\left\{-\frac{\hbar^2}{2m} \frac{d^2}{dx^2} + \infty\right\} \psi_{III}(x) = -E\psi_{III}(x) \quad (5)$$

Since $E - \infty$ is equal to $-\infty$, the equation can be simplified,

$$\left\{-\frac{\hbar^2}{2m} \frac{d^2}{dx^2}\right\} \psi_{III}(x) = -\infty\psi_{III}(x) \quad (6)$$

Both sides can be divided by the constant ∞ , and since $\frac{1}{\infty}$ is zero, the solution for wavefunction in the region III is.

$$\psi_{III}(x) = 0 \quad (7)$$

Region I solution

The Schrödinger equation in region I is

$$\left\{-\frac{\hbar^2}{2m} \frac{d^2}{dx^2} + 0\right\} \psi_I(x) = -E\psi_I(x) \quad (8)$$

It is most convenient write the wavefunction in the trigonometric function form.

$$\psi_I(x) = A \sin kx + B \cos kx \quad (9)$$

With A, B and k arbitrary constants. Substituting in the Schrödinger equation,

$$-\frac{\hbar^2}{2m} \frac{d^2}{dx^2} \{A \sin kx + B \cos kx\} = -E\{A \sin kx + B \cos kx\} \quad (10)$$

Taking the second derivative on the left side and simplifying yield

$$\frac{\hbar^2 k^2}{2m} \{A \sin kx + B \cos kx\} = E \{A \sin kx + B \cos kx\} \quad (11)$$

And then,

$$\frac{\hbar^2 k^2}{2m} = E \rightarrow k = \frac{\sqrt{2mE}}{\hbar} \quad (12)$$

Region II solution

The Schrödinger equation for the region II is

$$\left\{ -\frac{\hbar^2}{2m} \frac{d^2}{dx^2} + V_0 \right\} \psi_{II}(x) = -E \psi_{II}(x) \quad (13)$$

The general solution in the region II can be written

$$\psi_{II}(x) = C e^{\lambda x} + D e^{-\lambda x} \quad (14)$$

Where C, D are arbitrary constant and λ is a real positive constant. Substituting $\psi_{II}(x)$ in the Schrödinger equation.

$$\left\{ -\frac{\hbar^2}{2m} \frac{d^2}{dx^2} + V_0 \right\} (C e^{\lambda x} + D e^{-\lambda x}) = -E (C e^{\lambda x} + D e^{-\lambda x}) \quad (15)$$

Moving the constant terms that is multiplying the wavefunction to the right side, taking the second derivative and simplifying yields

$$-\frac{\hbar^2 \lambda^2}{2m} (C e^{\lambda x} + D e^{-\lambda x}) = (E - V_0) (C e^{\lambda x} + D e^{-\lambda x}) \quad (16)$$

Then,

$$-\frac{\hbar^2 \lambda^2}{2m} = (E + V_0) \Rightarrow \lambda = \frac{\sqrt{2m(V_0 + E)}}{\hbar} \quad (17)$$

Because the wavefunction must be finite, it must be tested to ensure that it does not blow up as $x \rightarrow \pm\infty$. In the region II, the first term $Ce^{\lambda x}$ blows up when $x \rightarrow \infty$ and makes the wavefunction in this region blow up, reducing the equation to

$$\psi_{II}(x) = De^{-\lambda x} \quad (18)$$

Boundary conditions

Since the potential is infinite in region III, only the wavefunction must be continuous across the boundary between region I and III ($x = 0$).

$$\psi_{III}(0) = \psi_I(0) \quad (18)$$

Substituting in the equation for the wavefunction in regions I and III gives $B = 0$. Therefore, the continuity requirement leads to:

$$\psi_I(x) = A \sin kx \quad (19)$$

At $x = L$ the wavefunction in the region I and II, and its first derivative must be continuous across the boundary.

$$\begin{aligned} \psi_I(L) &= \psi_{II}(L) \\ \psi'_I(L) &= \psi'_{II}(L) \end{aligned} \quad (20)$$

Dividing $\psi_I(L)$ by $\psi'_I(L)$ and $\psi_{II}(L)$ by $\psi'_{II}(L)$

$$\frac{A \sin kL}{Ak \cos kL} = \frac{De^{-\lambda L}}{-D\lambda e^{-\lambda L}} \quad (21)$$

Cancelling the constants A and D, the equation becomes

$$\lambda = -k \cot kL \quad (22)$$

Or

$$\cot \left\{ \frac{\sqrt{2m_{GaAs}m_e E}}{\hbar} L \right\} = - \sqrt{\frac{m_{GaAs}}{m_{AlGaAs}} \frac{E}{(V_0 + E)}} \quad (23)$$

Where, m_{GaAs} and m_{AlGaAs} are coefficient of the effective mass for the GaAs and AlGaAs, m_e is the electron mass, E is the energy of the confined state, V_0 the potential difference, L is the thickness of GaAs and \hbar is the Planck constant. Using 0.0632 and 0.0909 values [36] as m_{GaAs} and m_{AlGaAs} respectively and solving numerically the equation 23 is possible to find the energy of the confined state below the conduction band energy of the AlGaAs, in function of the GaAs thickness. If the found energy value is negative, the electron is confined. The used code was adapted to IgorPro from the Suwit Kiravitaya Matlab codes. See APPENDIX – I – Used code for particle in the box.

More sophisticated calculation was done with Nextnano³ software. Nextnano is a commercial package for the simulation of electronic and optoelectronic devices. The software solves the $k \cdot p$ perturbation theory and the Poisson equation to calculate the band gap diagram and the electron density of the structure. The entering parameter was the shape of the structure, doping concentration and the Schottky barrier. Figure 2.13 shows the used structure model for the Nextnano simulation. Cross-section TEM image (Figure 3.1) was used as template to create this simple trapezoid model. The orange bottom side represents the GaAs hole template, yellow part represents the 20nm AlGaAs barrier, and the orange top side represents the GaAs thickness used to fulfilled the holes. We assume the concentration of 3.0×10^{14} of carbon doping layer and a Schottky barrier pinned at 0.7eV. The used code is attached in APPENDIX – II – Used code for band diagram and electron density calculations.

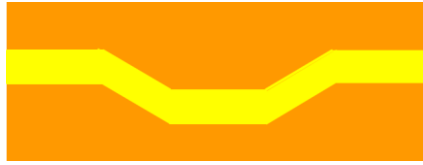


Figure 2.13: Structure model used for Nextnano simulation. The structure shape was simplified according to the TEM image, and representing the GaAs hole template (orange bottom side) covered with AlGaAs barrier (yellow) and fulfilled with GaAs (orange top side).

3. Development and results discussion

In this work, we used the Kelvin probe force microscopy (KPFM) to explore the nano-electrostatic properties of strain-free mesoscopic GaAs structures (MGS). The structures were fabricated by overgrowing a nanohole template using molecular beam epitaxy [1]. Therefore, the combination of Ga assisted deoxidation and local hole etching is used to create initial holes with a depth of ca. 10 to 15nm, which were covered subsequently with AlGaAs changing the concentration of Al and filled with GaAs of different thicknesses. The local potential and charge distribution in these structures was investigated using single pass KPFM. The NextNano3 software package was used to calculate band bending and electron wave function of the MGS.

3.1. Sample processing

The entire sample used in this work were grown by molecular beam epitaxy (MBE) at Brazilian Nanotechnology National Laboratory (LNNano). In this equipment is possible to growth epitaxially thin films of the III – V elements of periodic table. The current setup has four effusion cells (Ga, As, In, Al) and two doping cells (Si and Be) to grow high quality semiconductor heterostructures.

For the sample preparation, two different techniques were combined in order to produce the templates for unstrained quantum dots. In the first moment, Gallium assisted deoxidation technique removed the native gallium oxide (Ga_2O_3) from the top of GaAs (001) substrate. In this procedure, a Gallium atmosphere is used to react with the Ga_2O_3 generating Ga_2O (not stable). After the complete removal of native gallium oxide, the local droplet etching is used to produce the hole templates on top of the substrate. In this process, the exceed Gallium of deoxidation process, start to produce droplets on top of the substrate. The droplets in presence of low pressure of As will react with the surface of GaAs producing holes. The result is a homogeneous template of holes with ~ 20nm depth that was used to produce the unstrained QDs or mesoscopic GaAs structure (MGS).

With the hole template in hand, the first step to grow the MGS structure is filled the holes with AlGaAs. A few layer of AlGaAs will work as a potential barrier for carrier confinement of the QDs. In this study, we systematically used different thickness of AlGaAs barrier (15nm and 20nm) and changed the Al concentration of 33%, 50%, 70% and 90%. Then different thickness of GaAs was grown on top of the barrier. For the Kelvin probe measurements we stop the growth at this point because is necessary to access the center of the structure. The final MGS structure have one more layer of AlGaAs barrier and a GaAs cap to protect the structures as showed in the cross-section transmission electron microscopy (TEM) of the structure (Figure 3.1). For this measurement, the focus ion beam (FIB) technique was employed to cross-sectioned right on the middle of the structure.

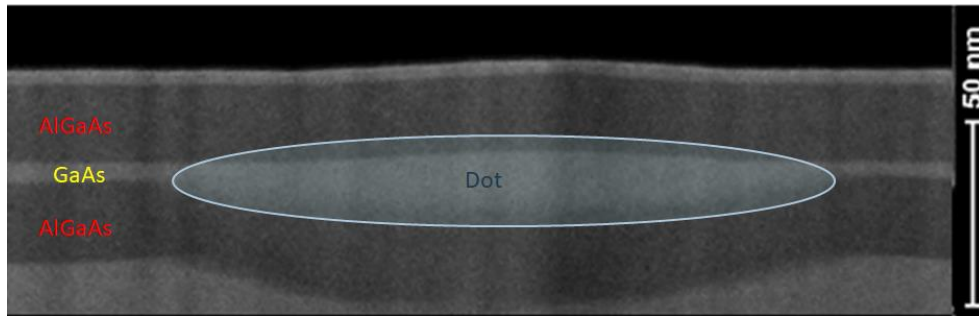


Figure 3.1: Cross-section transmission electron microscopy (TEM) of the strain-free quantum dots. The bright color shows the GaAs material and the dark color shows the AlGaAs material. The confinement potential gave by the dot formation is marked in the middle of the structure.

In Figure 3.2 we cannot see any dislocation or defects of the crystal in the AlGaAs/GaAs/AlGaAs junction of the sample. The dark region shows the AlGaAs barrier and the bright region is the GaAs layer. This is an important information for optical application, where is necessary high quality crystal for optical emission. In the same way, if we have dislocation or defects at the junction between the two semiconductors the charge carrier transport will change, modifying the quantum confinement.

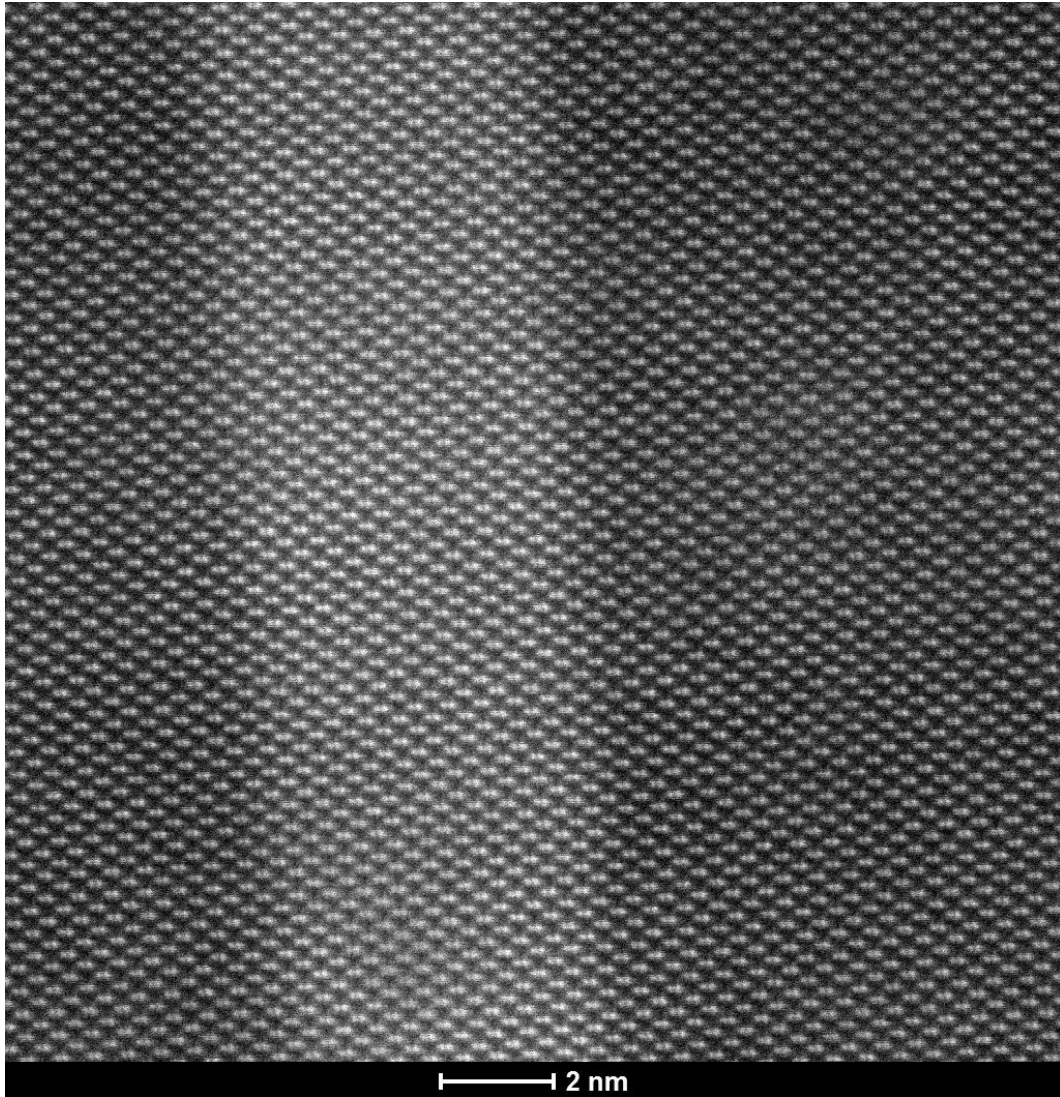


Figure 3.2: High-resolution transmission electron microscopy HR-TEM of the AlGaAs/GaAs/AlGaAs heterojunction cross-section. The dark and bright regions show the AlGaAs barrier and the GaAs layer respectively. No dislocation or defects is observed in this region of the sample, where the atoms made a perfect crystal.

In this work, we prepare a set of samples to comprehend the charge accumulation, following the steps above and outlined in Figure 2.1:

- (I) Only holes made by LDE
- (II) Holes filled with AlGaAs barrier
- (III) Holes filled with AlGaAs barrier and changing the amount of GaAs
- (IV) Holes filled with AlGaAs barrier and GaAs but changing the Al concentration



Figure 3.3: Schematic showing set of the analyzed sample. (I) only substrate with GaAs holes; (II) holes with AlGaAs barrier; (III) holed with AlGaAs barrier and changing GaAs thickness; (IV) holes with different concentration of Aluminum in the AlGaAs barrier and filled with 2nm GaAs.

3.2. Kelvin probe force microscopy measurements

In the Figure 3.4 the measurement of initial holes template is showed. We use this image to confirm that the observed difference potential in the final structure is not coming from topography artifacts.

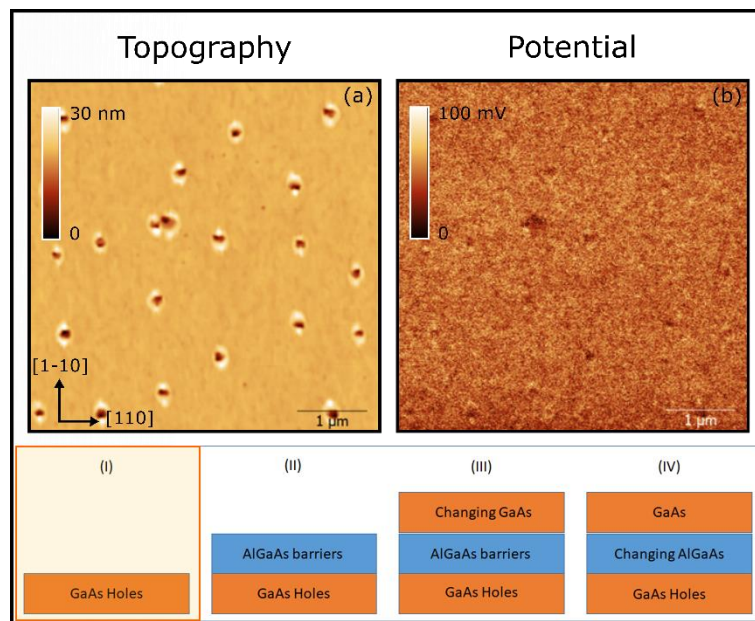


Figure 3.4: Topography (a) and KPFM (b) images of the template holes. Depth of the holes is around 15nm. The electrostatic potential is homogenous under the surface.

Figure 3.4 (a) shows the topography of GaAs substrate with the hole templates. The gallium droplets etching make holes with 20nm depth approximately. As showed in section 2.2 an expected GaAs accumulation with 5nm height is observed beside the holes and following the substrate orientation. The KPFM results is shown in Figure 3.4 (b). The electrostatic surface potential is uniform over the sample since we have only GaAs over the surface. This result proofs that the irregular topography of the structure is not generating artifacts to the potential data.

In the second set of sample, we grown 20nm of $Al_{0.33}Ga_{0.67}As$ barrier was deposit over the hole template and measured in the same way (Figure 3.5).

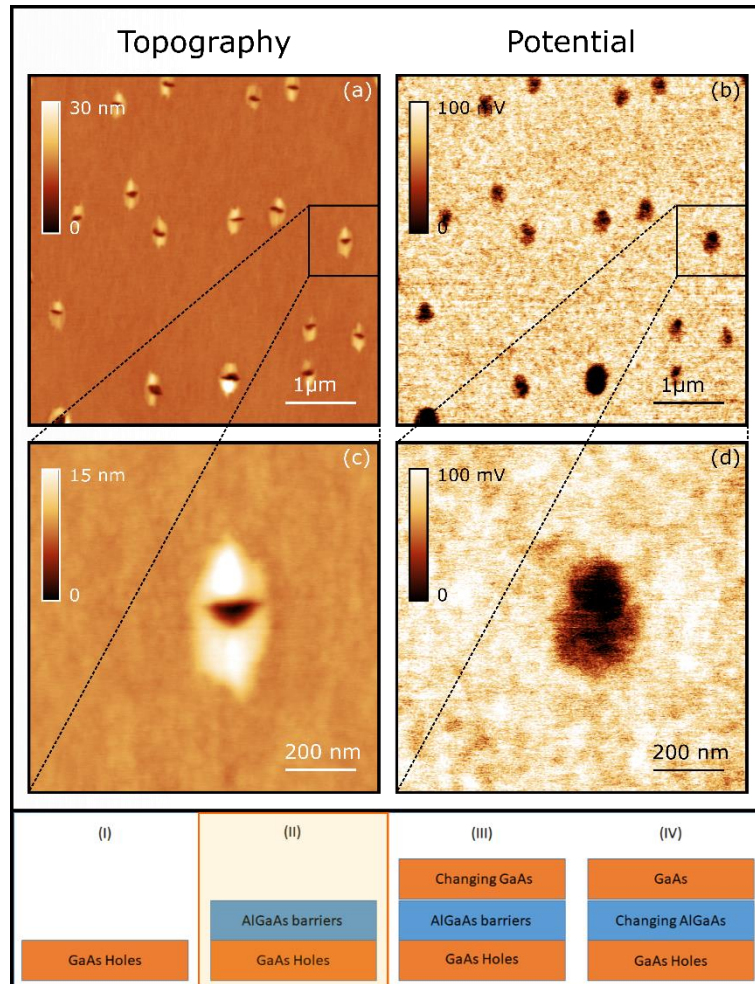


Figure 3.5: Topography (a, c) and KPFM (b, d) of the hole template after 15nm AlGaAs barrier deposition. The topography looks similar to the initial hole template indicating AlGaAs follow

evenly the shape of the holes. The potential data shows difference electrostatic potential over the structures, with higher contrast in the mounts beside the holes.

Figure 3.5 shows the topography (a, c) and KPFM (b,d) results of these structures. As observed on Figure 3.4, the topography does not change so much from the initial hole template. This behavior indicates an epitaxial and uniform growth of the AlGaAs barrier, by following the shape of the holes. From the KPFM result, we observe a huge difference in the electrostatic surface potential. Regions with the structures relief (mounts and hole) shows lower electrostatic potential, but the mounts region have higher contrast if compared with the holes region. A suggestion for the observed effect is because an “inverted” quantum dot formed over the mounts around the hole.

The Figure 3.6 shows a set of images from MGS structures. We used the holes template showed in Figure 3.4 and deposit 20nm of $\text{Al}_{0,33}\text{Ga}_{0,67}\text{As}$ and 2nm of GaAs.

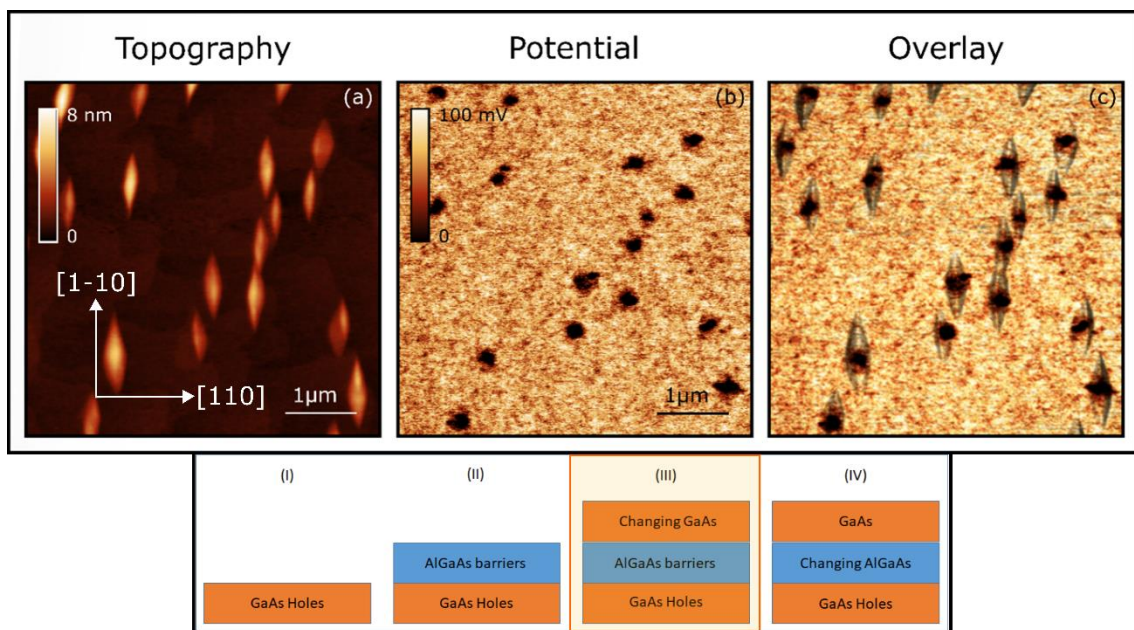


Figure 3.6: Difference electrostatic potential observed on MGS structures. (a) Topography showing the shape of the unstrained quantum dots. (b) KPFM measurement showing a contrast

right on the middle of the structures (holes template). (c) Overlay topography and KPFM data to identify the exactly position where we observe the contrast in electrostatic potential.

Topography images shows an elongation of the structure in the direction [1-10] due the preferential material diffusion (Figure 3.6 (a)). The GaAs completely filled the initial holes generating a region with higher mounts (height distribution of 5.05nm Figure 3.7) and dimensions around 800nm x 200nm. KPFM measurements shows a contrast in the potential data (Figure 3.6 (b)). The black spots region means that surface potential at the MGS region is lower than surrounding. An overlay (Figure 3.6 (c)) confirm that the difference at the potential data is situated right at the middle of the structures, where we expected the holes are. This results indicates a charge confinement inside the MGS structures but only at the hole position. Afterwards, we prepared samples with different amount of GaAs.

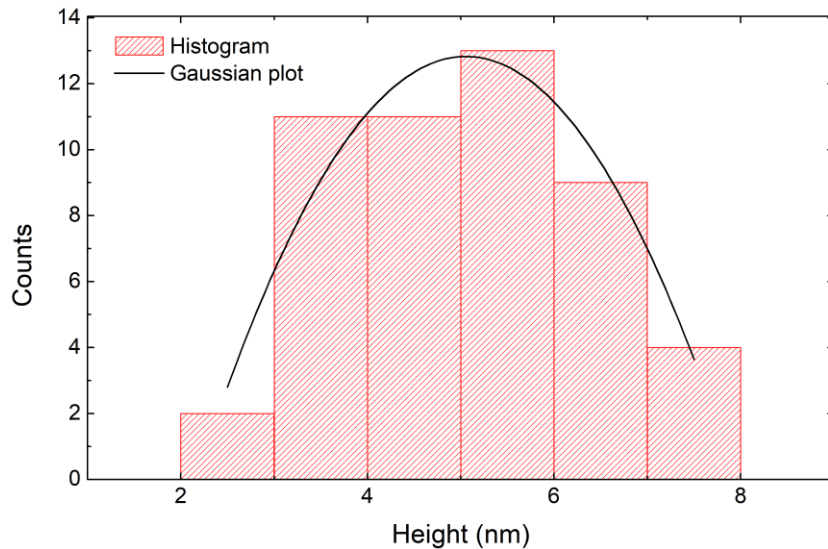


Figure 3.7: Height histogram of the sample with 2nm thickness of GaAs. The red color shows the number of counts in each height of the structure. Black curve is the Gaussian plot of the histogram with maximum value 5.05nm.

3.3. Changing GaAs thickness

After observed the charge accumulation inside the MGS structure, we prepare of samples to check the confinement when changing the GaAs layer thickness. Figure shows topography and potential data for 1nm, 2nm, 5nm and 10nm thickness of

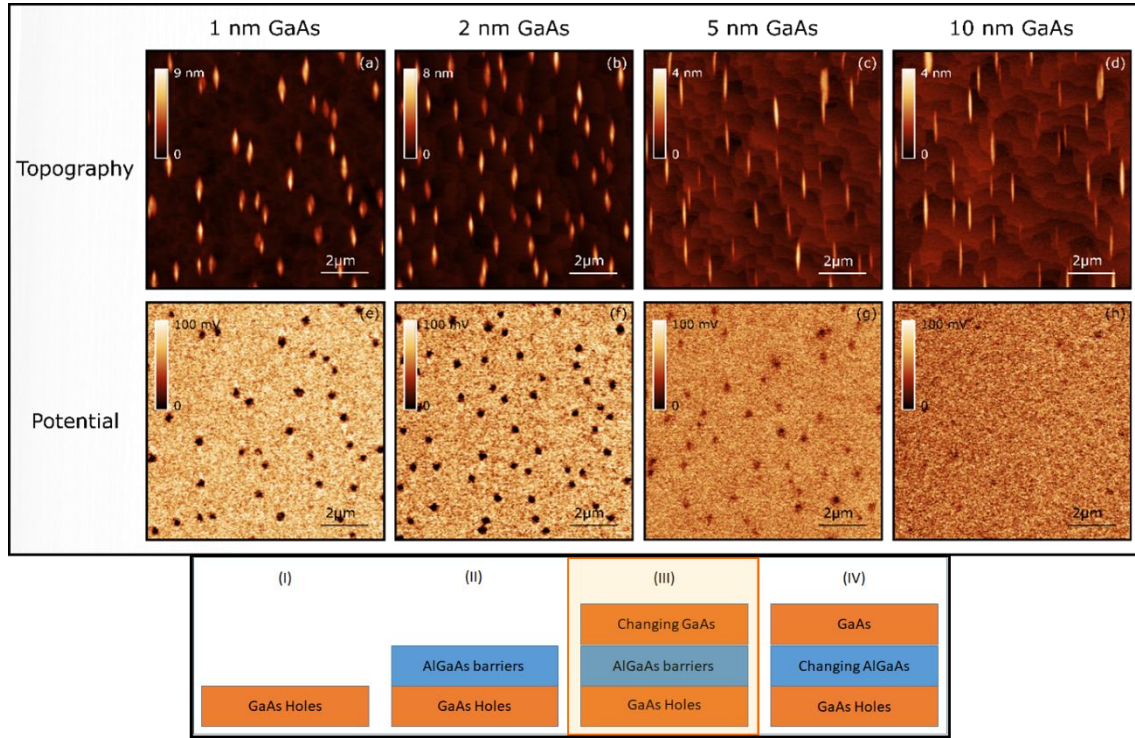


Figure 3.8: Topography (a-d) and KPFM (e-h) images acquired for different thickness of GaAs. The structures elongate when the thickness was increased and the difference electrostatic potential disappear with 10nm thickness of GaAs.

The images (Figure 3.8 (a-d)) shows the topography image for different thickness of GaAs. We observed a higher elongation of the structures and a decrease in height when the thickness increases. With increasing GaAs layer thickness covering the hole-mound structures, the height distribution for this sequence of samples was 6.6nm 5.05nm, 2.2nm and 2.7nm respectively for 1nm, 2nm, 5nm and 10nm thickness of GaAs. These topographical images is illustrating that the [1-10] direction grows faster than the [110] direction. This effect was already observed by Silva et.al. [1], where the asymmetric Ga surface diffusion during the hole formation, result in an increased growth rate in the [1-10] direction of the

crystal. Hence, the structures does not symmetrically flatten out as naively expected, but flattens by elongation in one direction and by continuously decreasing the mound height over the surrounding flat GaAs surface.

On the other hand, the Figure 3.8 (e-f) show the KPFM results when changing the thickness of GaAs. For the sample with 1nm and 2nm thickness we observed a surface potential contrast around 100mV between the structure and the surrounding. The contrast is reduced when the GaAs thickness increase to 5nm and is close to zero when increase to 10nm.

3.4. Changing aluminum concentration into AlGaAs barrier

Samples with different concentration of Aluminum in the AlGaAs barrier were measured. Changing the concentration of Al into the barrier the band gap will change and consequently the carrier confinement will change. The Figure 3.9 shows the topography (a-d) and KPFM (e-h) measurements of the samples with different concentration of Al. In the topographical images of the 0.3, 0.5 and 0.7 Aluminum content, is possible to identify the MGS structures as before, with the AlGaAs barrier following the hole shape. However, for 0.9 Aluminum content, we observed a huge change in the topographical images. The change in topographical image is because the Aluminum easily oxidizes under ambient condition, and as higher is the Al content, easily oxidation is observed for these samples without the GaAs layer.

The Figure 3.9 (e-h) shows the potential maps for these structures. For 0.3, 0.5 and 0.7 contents, a clear contrast between the MGS structures and the surrounding was observed in the potential data, with the 0.5 Al content showing the higher contrast. Lower contrast is observed for the 0.7 in comparison to 0.5 probably due the direct-to-indirect transition of the band gap. In the 0.9 content, the sample surface oxidized as observed in the topographical images, for this reason the surface potential is homogenous over the surface. In other words, no confinement is archived with the complete oxidation of the surface.

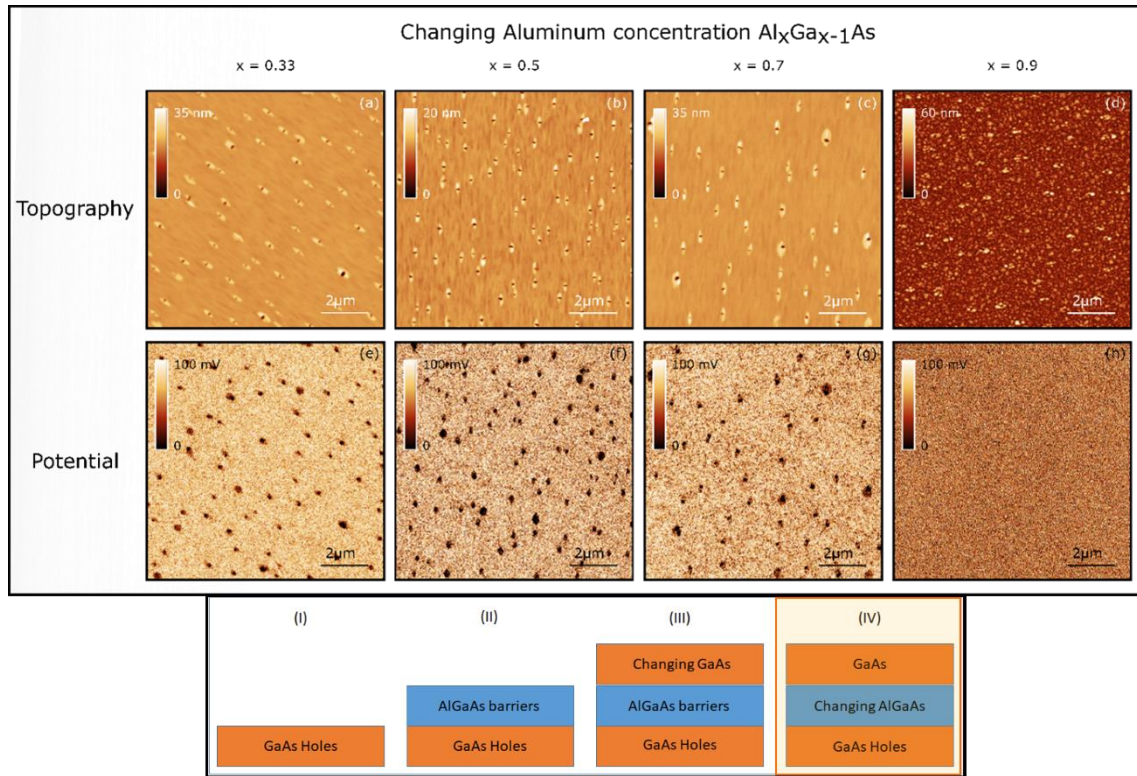


Figure 3.9: Topography (a-d) and KPFM (e-h) measurement of the holes with $\text{Al}_x\text{Ga}_{x-1}\text{As}$ barrier in different concentration of Aluminum. The images with $x = 0.3, 0.5, 0.7$ shows black spots in potential data. The concentration 0.9 looks like oxidized surface and does not show any contrast in potential data.

3.5. Modelling half-finite quantum well

3.5.1. Numerical solution

Assuming that the observed signal measured in our samples behave as a particle in a half-finite quantum well, we solve the classical equation for a potential deep to calculate the energy difference between the valence and conduction band in the confined state. We compare the energy solution for the finite and half-finite quantum well. In Figure 3.10a and Figure 3.10b is outlined the finite both sides quantum well and the half-finite quantum well, respectively, formed by the AlGaAs/GaAs heterostructure. Figure 3.10.d shows the energy plot for both conditions. The energy is plotted relatively to the conduction band of the AlGaAs and let the electron drop into the potential deep. Therefore the calculated energy gives

the energy of the confined state below the conduction band energy of AlGaAs - if it is negative, the electron is confined. Thus, from this plot, if the GaAs thickness is lower than 1.5nm no confinement is observed. With this theoretical results we change the sample processing in the way that the GaAs follow the shape of the holes as showed in the schematic of Figure 3.10c.

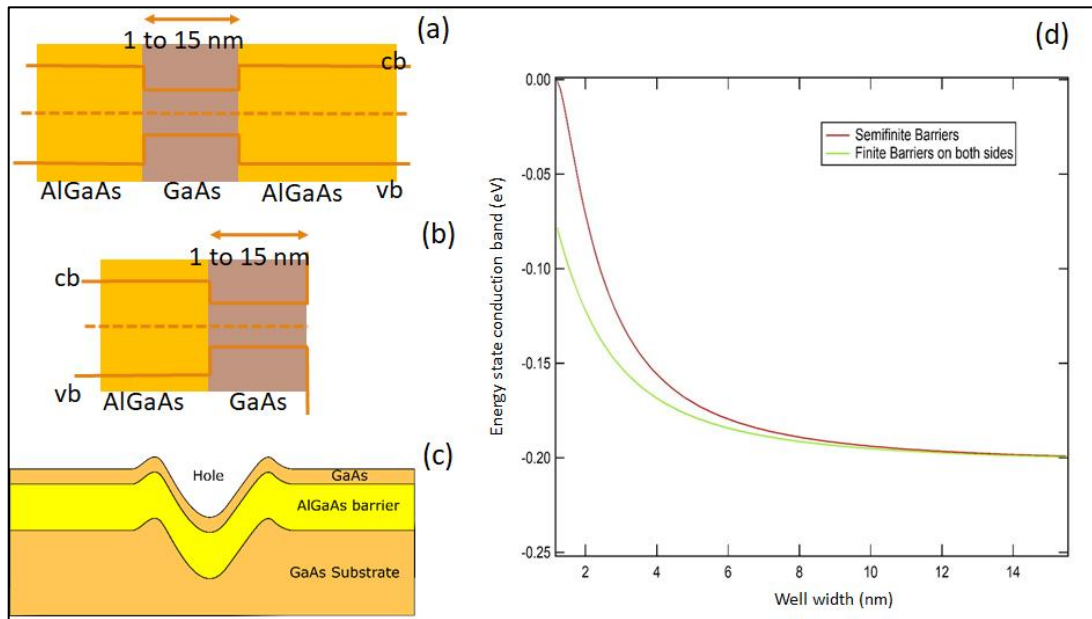


Figure 3.10: Modelling the finite and the half-finite quantum-well. (a) General schematic for a quantum well (a) finite barrier of both sides and (b) half-finite. (c) Schematic of the grown sample. (d) Simulation of the energy in function of the well width.

3.5.2. KPFM of the proposed sample

Figure 3.11 shows the samples grown with 1nm and 2nm thickness of GaAs and following the schematic of Figure 3.10c. To the GaAs follow the hole shape is necessary to abrupt cooling down the temperature of the sample after grow. Doing this the GaAs will follow the shape of the hole template. The topography image of these samples is showed in Figure 3.11(a-b). From the topography, we see the hole shape is still preserved, indicating that GaAs layer is following the hole template. In the potential data, the sample with 1nm (Figure 3.11c) thickness of GaAs doesn't show any contrast, while, the sample 2nm thickness of GaAs show a clear contrast between the holes and the surrounding. These results are in agreement with our calculations where thickness lower than 1.5nm does not confine any charge.

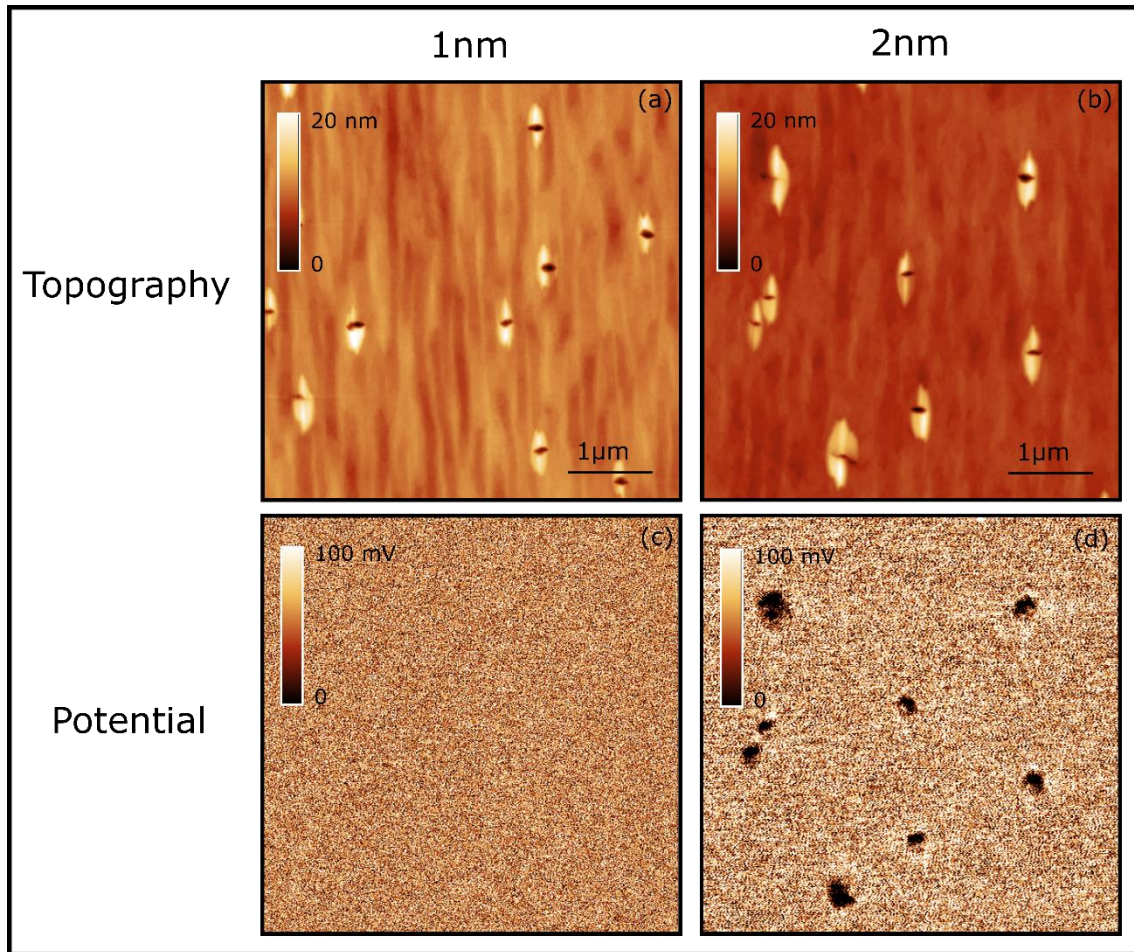


Figure 3.11: Structures grown following the hole template. Topography image for (a) 1nm and (b) 2nm GaAs thickness. The potential image for (c) 1nm doesn't show any contrast and for (d) 2nm shows a clear contrast.

3.6. Simulations of band diagram and electron wave function

The Nextnano3 software package was used to simulate the band diagram (Figure (Figure 3.12) and the electron wave function (Figure 3.13) of the MGS structures.

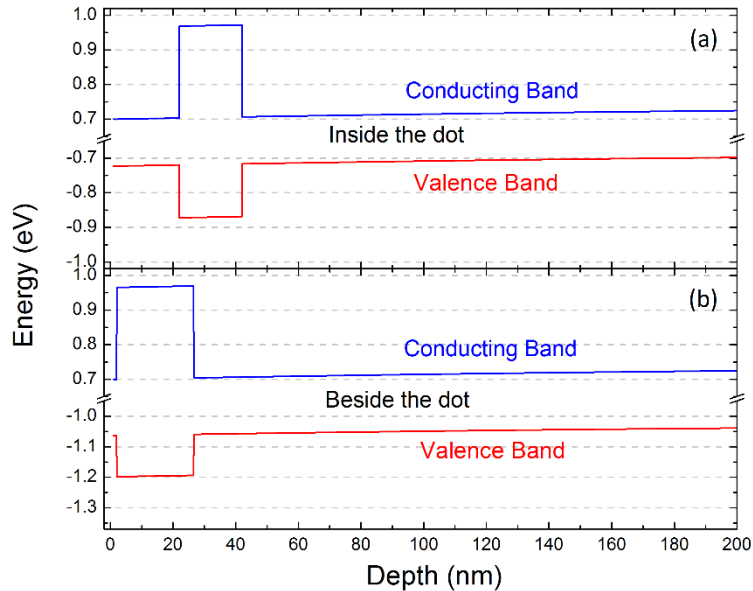


Figure 3.12: Band diagram of the unstrained quantum dot. The conduction and valence band was plotted (a) inside and (b) beside the dot. In both graph a small band bending was observed due the fermi level pinning.

The conducting and valence band inside and beside the dots were plotted in Figure 3.12. In both cases we observe a band bending of the conduction and valence band, indicating the Fermi level pinning phenomena caused by surface potential in the interface. This band bending makes possible a charge accumulation inside the dots, with the electron moving for states with lower energies close to the surface. For this kind of system, we should naturally see a charge accumulation in the AlGaAs barrier, but when we applied the AC voltage, used during KPFM measurements, this behavior was intensified.

The Figure 3.13 shows the electron wavefunction calculation changing the thickness of GaAs. When using 2nm GaAs thickness the green spot is not dispersed, in other words, electron intensity is more localized indicating a higher probability of charge accumulation.

This simulation follows according to the experimental results when we observe a higher charge accumulation decreasing the GaAs thickness.

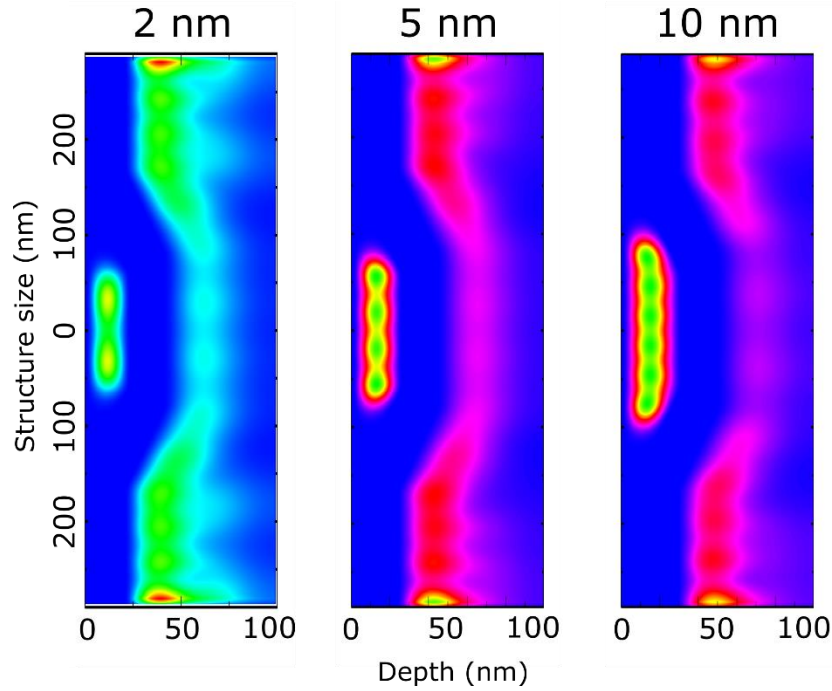


Figure 3.13: Electron probability simulation of the unstrained quantum dot. Increasing the thickness of the GaAs the probability of the electron dissipate over the sample increase.

3.7. Electrostatic force microscopy (EFM) without AC voltage

Electrostatic force microscopy (EFM) was done for the sample with 50% Aluminum content and 2nm GaAs thickness. The Figure 3.14a-b show the topography image of the sample and the Figure 3.14c-d show the EFM phase signal at the same region using 20nm and 100nm lift. Using 100nm lift, we see only a small bright dot in the EFM image that comes from surface contamination, also observed in the topography image. When the lift is reduced to 20nm, we start to see some contrast in the EFM image, which is not a real EFM contrast. As described in the Chapter 2, the EFM technique works in lift mode and without AC voltage applied between tip and sample. In this way, the tip is always keeping a constant distance to

the sample surface, and, when far enough, the tip is probing only the electrostatic forces and not the Van der Waals interaction. Therefore, if we look carefully for the EFM image with 20nm lift, we see that always in the left side of the structure the contrast is dark, and the left side in bright. These facts are an indicative that the EFM signal is contaminated with the Van der Waals/topography information, where the signal move to one side when the tip moves up and to the other side when tip moves down.

From the previous KPFM results, we expect to see charge accumulation right on the middle of the MGS structures. However, for the EFM measurement (Figure 3.14c-d) no clear difference potential signal was observed for this sample. The explanation for this behavior is because, at this condition, we are not applying to the tip, the AC voltage used in the KPFM technique. We suggest, that the AC voltage are inducing charges on the sample surface, which, due to the different band gap of the material, immediately confine inside the MGS structures.

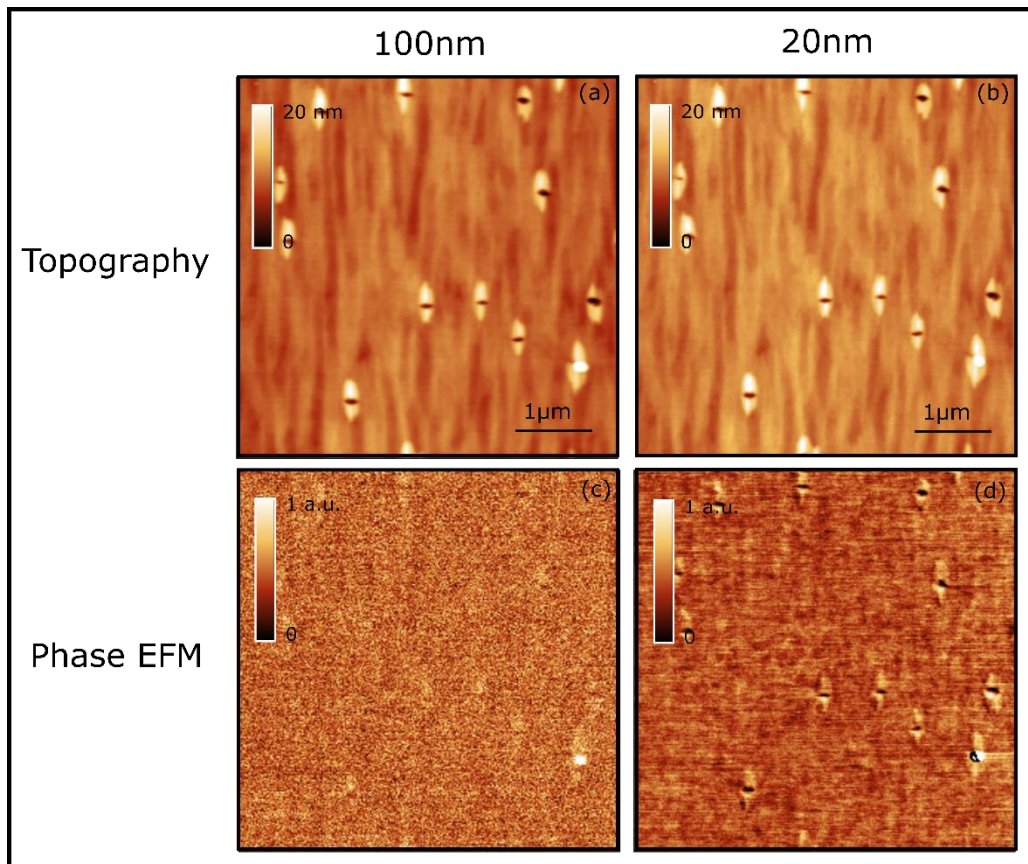


Figure 3.14: Topography images (a-b) of the sample with 0.5 Aluminum content and 2nm GaAs thickness. EFM phase signal (c-d) with 100nm and 20nm lift respectively. No clear

contrast is observed for the 100nm lift (c). The shallow contrast for 20nm lift (d) is due the tip fell the Van der Waals interaction, and should not be consider as a real signal.

4. Conclusions

The analyzed samples allowed to access the internal region of the mesoscopic GaAs structures and measure their electrostatic properties. Kelvin probe measurement demonstrates a huge capability to direct probe difference in the electrostatic surface potential with nanometric resolution.

The observed charge accumulation was right on the middle of the structures where we expect the holes are. This is due to the difference band gap of the materials that produce a carrier confinement similar to a particle in the box. In the first set of sample, when changing the GaAs thickness, we observed that the difference potential between the MGS structures and the surrounding is higher for 2nm GaAs thickness. Increasing the GaAs thickness, we observe the difference potential reducing, because lower confinement is archived as thicker is the GaAs.

Changing the Aluminum content, second set of samples, we observed a complete oxidation of the surface for Al concentration in 90%. The oxidation interfere in the KPFM measurement where no difference potential at the holes were observed. The sample with Al concentration around 50% present higher difference band gap compared to the 30%. For this reason we see higher difference potential in this sample. The same reasoning cannot be followed for the sample with 70% Al concentration because the sample probably start the oxidation process.

Forcing the GaAs layer to follow the shape of the hole template we observe no charge accumulation inside the structures for the 1nm GaAs thickness. This result corroborate with the simulation of the half-finite quantum well where no confinement is observed for 1nm thickness.

The simulations using NextNano package software held us to better describe the charge accumulation. The band diagram shows a band bending with lower values close to the surface, making possible the charge accumulation. The electron density plot, move in the same direction of the experimental data, with better confinement for the 2nm GaAs structures.

Electrostatic force microscopy (EFM) in lift mode shows that the huge signal observed in the KPFM measurement is intensified by the AC voltage applied to the tip. This voltage is inducing charges on the sample surface, which gets confined due the band gap difference of the materials.

5. Bibliographical References

- [1] S. F. C. da Silva, T. Mardegan, S. R. de Araújo, C. A. O. Ramirez, S. Kiravittaya, O. D. D. Couto, F. Iikawa, and C. Deneke, *Nanoscale Res. Lett.* **12**, (2017).
- [2] S. Okamura, *History of Electron Tubes* (IOS Press, 1994).
- [3] T. Belhadj, T. Kuroda, C.-M. Simon, T. Amand, T. Mano, K. Sakoda, N. Koguchi, X. Marie, and B. Urbaszek, *Phys. Rev. B* **78**, 205325 (2008).
- [4] C. Heyn, A. Stemmann, T. Köppen, C. Strelow, T. Kipp, M. Grave, S. Mendach, and W. Hansen, *Nanoscale Res. Lett.* **5**, 576 (2009).
- [5] S. F. C. da Silva, E. M. Lanzoni, V. de A. Barboza, A. Malachias, S. Kiravittaya, and C. Deneke, *Nanotechnology* **25**, 455603 (2014).
- [6] B. A. Joyce and T. B. Joyce, *J. Cryst. Growth* **264**, 605 (2004).
- [7] D. Bimberg, M. Grundmann, F. Heinrichsdorff, N. N. Ledentsov, V. M. Ustinov, A. E. Zhukov, A. R. Kovsh, M. V. Maximov, Y. M. Shernyakov, B. V. Volovik, A. F. Tsatsul'nikov, P. S. Kop'ev, and Z. I. Alferov, *Thin Solid Films* **367**, 235 (2000).
- [8] N. N. Ledentsov, *Semiconductors* **33**, 946 (1999).
- [9] Ivan N. Stranski and Lubomir Krastanow, *Abh. Math.-Naturwissenschaftlichen Kl. Iib Akad. Wiss. Wien* **146**, 797 (1938).
- [10] P. Bhattacharya, S. Ghosh, and A. D. Stiff-Roberts, *Annu. Rev. Mater. Res.* **34**, 1 (2004).
- [11] I. Kegel, T. H. Metzger, A. Lorke, J. Peisl, J. Stangl, G. Bauer, J. M. García, and P. M. Petroff, *Phys. Rev. Lett.* **85**, 1694 (2000).
- [12] A. Rastelli, S. Stufler, A. Schliwa, R. Songmuang, C. Manzano, G. Costantini, K. Kern, A. Zrenner, D. Bimberg, and O. G. Schmidt, *Phys. Rev. Lett.* **92**, 166104 (2004).
- [13] S. Kiravittaya, A. Rastelli, and O. G. Schmidt, *Rep. Prog. Phys.* **72**, 046502 (2009).
- [14] A. Stemmann, C. Heyn, T. Köppen, T. Kipp, and W. Hansen, *Appl. Phys. Lett.* **93**, 123108 (2008).
- [15] Z. M. Wang, B. L. Liang, K. A. Sablon, and G. J. Salamo, *Appl. Phys. Lett.* **90**, 113120 (2007).
- [16] Y. H. Huo, B. J. Witek, S. Kumar, J. R. Cardenas, J. X. Zhang, N. Akopian, R. Singh, E. Zallo, R. Grifone, D. Kriegner, R. Trotta, F. Ding, J. Stangl, V. Zwiller, G. Bester, A. Rastelli, and O. G. Schmidt, *Nat. Phys.* **10**, 46 (2014).
- [17] N. Akopian, L. Wang, A. Rastelli, O. G. Schmidt, and V. Zwiller, *Nat. Photonics* **5**, 230 (2011).
- [18] A. Rastelli, F. Ding, J. D. Plumhof, S. Kumar, R. Trotta, C. Deneke, A. Malachias, P. Atkinson, E. Zallo, T. Zander, A. Herklotz, R. Singh, V. Krapek, J. R. Schroeter, S. Kiravittaya, M. Benyoucef, R. Hafenbrak, K. D. Joens, D. J. Thurmer, D. Grimm, G. Bester, K. Doerr, P. Michler, and O. G. Schmidt, *Phys. Status Solidi B-Basic Solid State Phys.* **249**, 687 (2012).
- [19] R. Trotta, P. Atkinson, J. D. Plumhof, E. Zallo, R. O. Rezaev, S. Kumar, S. Baunack, J. R. Schröter, A. Rastelli, and O. G. Schmidt, *Adv. Mater.* **24**, 2668 (2012).

- [20] J. Zhang, Y. Huo, A. Rastelli, M. Zopf, B. Höfer, Y. Chen, F. Ding, and O. G. Schmidt, *Nano Lett.* **15**, 422 (2015).
- [21] M. N. Makhonin, K. V. Kavokin, P. Senellart, A. Lemaître, A. J. Ramsay, M. S. Skolnick, and A. I. Tartakovskii, *Nat. Mater.* **10**, 844 (2011).
- [22] G. Sallen, S. Kunz, T. Amand, L. Bouet, T. Kuroda, T. Mano, D. Paget, O. Krebs, X. Marie, K. Sakoda, and B. Urbaszek, *Nat. Commun.* **5**, 3268 (2014).
- [23] A. Y. Cho and H. C. C. Jr, *Appl. Phys. Lett.* **25**, 288 (1974).
- [24] Z. I. Alferov, *Phys. Scr.* **1996**, 32 (1996).
- [25] K. Y. Cheng, *J. Vac. Sci. Technol. Vac. Surf. Films* **31**, 050814 (2013).
- [26] A. Morais, J. P. C. Alves, F. A. S. Lima, M. Lira-Cantu, and A. F. Nogueira, *J. Photonics Energy* **5**, 057408 (2015).
- [27] W. P. McCray, *Nat. Nanotechnol.* **2**, 259 (2007).
- [28] O. G. Schmidt, A. Rastelli, G. S. Kar, R. Songmuang, S. Kiravittaya, M. Stoffel, U. Denker, S. Stufler, A. Zrenner, D. Grutzmacher, B. Y. Nguyen, and P. Wennekers, *Phys. E-Low-Dimens. Syst. Nanostructures* **25**, 280 (2004).
- [29] X. Li, J. Wu, Z. M. Wang, B. Liang, J. Lee, E.-S. Kim, and G. J. Salamo, *Nanoscale* **6**, 2675 (2014).
- [30] P. Atkinson and O. G. Schmidt, *J. Cryst. Growth* **311**, 1815 (2009).
- [31] P. Tomkiewicz, A. Winkler, and J. Szuber, *Appl. Surf. Sci.* **252**, 7647 (2006).
- [32] Z. R. Wasilewski, J.-M. Baribeau, M. Beaulieu, X. Wu, and G. I. Sproule, *J. Vac. Sci. Technol. B Microelectron. Nanometer Struct. Process. Meas. Phenom.* **22**, 1534 (2004).
- [33] J. H. Lee, Z. M. Wang, and G. J. Salamo, *J. Appl. Phys.* **100**, 114330 (2006).
- [34] T. Mano and N. Koguchi, *J. Cryst. Growth* **278**, 108 (2005).
- [35] C. Heyn, *Phys. Rev. B* **83**, 165302 (2011).
- [36] E. H. Li, *Phys. E Low-Dimens. Syst. Nanostructures* **5**, 215 (2000).
- [37] G. Binnig, H. Rohrer, C. Gerber, and E. Weibel, *Appl. Phys. Lett.* **40**, 178 (1982).
- [38] G. Binnig, H. Rohrer, C. Gerber, and E. Weibel, *Phys. Rev. Lett.* **49**, 57 (1982).
- [39] G. Binnig, C. F. Quate, and C. Gerber, *Phys. Rev. Lett.* **56**, 930 (1986).
- [40] J. E. Stern, B. D. Terris, H. J. Mamin, and D. Rugar, *Appl. Phys. Lett.* **53**, 2717 (1988).
- [41] B. D. Terris, J. E. Stern, D. Rugar, and H. J. Mamin, *Phys. Rev. Lett.* **63**, 2669 (1989).
- [42] M. Nonnenmacher, M. P. O'Boyle, and H. K. Wickramasinghe, *Appl. Phys. Lett.* **58**, 2921 (1991).
- [43] D. W. Abraham, *J. Vac. Sci. Technol. B Microelectron. Nanometer Struct.* **9**, 703 (1991).
- [44] Y. Martin and H. K. Wickramasinghe, *Appl. Phys. Lett.* **50**, 1455 (1987).

- [45] D. Rugar, H. J. Mamin, P. Guethner, S. E. Lambert, J. E. Stern, I. McFadyen, and T. Yogi, *J. Appl. Phys.* **68**, 1169 (1990).
- [46] M. Saint Jean, S. Hudlet, C. Guthmann, and J. Berger, *J. Appl. Phys.* **86**, 5245 (1999).
- [47] O. A. Castañeda-Uribe, R. Reifenberger, A. Raman, and A. Avila, *ACS Nano* **9**, 2938 (2015).
- [48] W. Melitz, J. Shen, A. C. Kummel, and S. Lee, *Surf. Sci. Rep.* **66**, 1 (2011).
- [49] F. Galembeck and C. A. R. Costa, *Electric Scanning Probe Techniques: Kelvin Force Microscopy and Electric Force Microscopy*. (Marcel Dekker, New York, 2006).
- [50] M. A. Salem, H. Mizuta, and S. Oda, *Appl. Phys. Lett.* **85**, 3262 (2004).
- [51] M. Tanimoto and O. Vatel, *J. Vac. Sci. Technol. B* **14**, 1547 (1996).

APPENDIX – I – Used code for particle in the box

```
#pragma rtGlobals=3          // Use modern global access method and
strict wave access.

//Define a grenarl Constant

Constant PlanckConstantReduced=1.054571800e-34,electronmass=9.10938356e-
31,electroncharge=1.6021766208e-19
Constant eVtoJoul=1.602176565e-19

//Functions to calculate QW energy levels

//Material properties functions

Function AlGaAs_prop(Al_content,properties,[q])

//Calculates the band gap and electron masses for unstrained GaAs
//
// Based on a Mathematica sheet by Suwit
//
//Version 1.0 (27.01.2017)
//
// Materials parameters after E. H. Li, Physica E 5, 215 (200) and C. Van
de Walle, PRB 39, 1871 (1989)
// Li works with band offset theory and is not so clear, what is the
bandoffset ratio (should be 50:50 according to
// S. Achachi, GaAs and related materials (World Scientific)
// Suwit uses model-solid theory, which will provided a band position and
a spin-orbit coupling offset.
//
//Values to be written in properties wave
//properties[1]: Bandgap
//properties[2]: Energy Valence band
//properties[3]: Energy Conduction band
//properties[4]: Mass electrons
//properties[5]: Mass heavy holes

Wave/D properties
Variable Al_content,q

//Define soem internal variables

Variable evav,delta

evav=-6.92*(1-Al_content)-7.49*Al_content //model-solid valenceband
energy at delta point after PRB
delta=0.341-0.066*Al_content // Spin-orbit splitting after Li for the
valence band (our zero)

properties[0]=1.5194+(1.36*Al_content)+(0.22*Al_content^2) //Bandgap at
low temp after Li
properties[1]=evav+delta/3 //Position of the valence band for given
concentration - Valence band has an average position and a splting due to
spin orbit
properties[2]=properties[0]+properties[1] // The conduction band energy
is valenceband energy plus band gap
properties[3]=0.0665+(0.1006 * Al_content)+(0.0137*Al_content^2)
```

```

properties[4]=0.34+0.16*Al_content

//Print results if q=0

if( ParamIsDefault(q))
printf "Bandgap: %g\r", properties[0]
printf "Valenceband energy: %g\r", properties[1]
printf "Conduction band energy: %g\r", properties[2]
printf "Electron mass: %g\r", properties[3]
printf "Heavy hole mass: %g\r", properties[4]
endif

End

Function Symteric_finiteQW(coeff,x)

// Condition for symetric solution of a QW after Suwit. Zero is the
barrier and the carries are confined by a negative energy inside the well
dip.
//
// To find theEnergylevel, this function has to return zero
//
// coeff[0]: Potential difference
// coeff[1]: Mass carrier in Well
// coeff[2]: Mass carrier in Barrier
// coeff[3]: thickness of the QW

Wave/D coeff
Variable x

Variable left,right,k,kappa

//k=sqrt((2*coeff[1]*electronmass*x*eVtoJoul)/PlanckConstantReduced^2)
//kappa=sqrt((2*coeff[2]*electronmass*(coeff[0]-
x)*eVtoJoul)/PlanckConstantReduced^2)

//left=tan(0.5*k*coeff[3]*1e-9)
//right=kappa/k

left=tan(0.5*coeff[3]*1e-
9*(sqrt(2*coeff[1]*electronmass*(coeff[0]+x)*eVtoJoul)/PlanckConstantRedu
ced))
right=sqrt(coeff[1]/coeff[2]*(-x/(coeff[0]+x)))

return left-right

End

//-----
//-----
//-----

Function semifinite_QW(coeff,x)

// Condition for symetric solution of a QW after Suwit and modifit for a
hakf infinit barrier. Zero is the barrier and the carries are confined by
a negative energy inside the well dip.
// Difference is only to take away a factor of two before and we have to
use the cotan instead of tan.

```

```

//
// To find theEnergylevel, this function has to return zero
//
// coeff[0]: Potential difference
// coeff[1]: Mass carrier in Well
// coeff[2]: Mass carrier in Barrier
// coeff[3]: thickness of the QW

Wave/D coeff
Variable x

Variable left,right

left=cot(coeff[3]*1e-
9*(sqrt(2*coeff[1]*electronmass*(coeff[0]+x)*eVtoJoul)/PlanckConstantRedu
ced))
right=-sqrt(coeff[1]/coeff[2]*(-x/(coeff[0]+x)))

return left-right
//return left

End

//-----
//-----
//-----

Function AlGaAs_semifiniteQW_transition(al_content,thickness,[q])

//Calculates the transition energy in an unstrained AlGaAs/GaAs Qw
assuming semifinite barrieres of infinite thickness and a QW thickness
// One side has infinite potential, the other side has an AlGaAs barrier
//
//Fuinction follows Suwits Mathematica sheet
//
//Version 1.0 27.01.2017
//
//returns transition energie and needs Al content of Barrier and GaAs
thickness as input
//
// Eq. for QW can be found inS. Adachi, GaAs and Related Materials, World
Scientific
// The given solution is wrong after Suwit and Wikipedia
//

Variable al_content,thickness,q

Variable V0, Elc,Elv, lower

Make/D /N=10 propertiesQW,propertiesbarrier,coeff

AlGaAs_prop(0,propertiesQW,q=1)
AlGaAs_prop(al_content,propertiesbarrier,q=1)

//calculate energy state of the vallence band

coeff[0]=0.57*(propertiesbarrier[0]-propertiesQW[0]) //Band discontinuety
or confinement potential of conduction band using band gap nand band
offset ratios (ca. 0.5) from literature

```

```

//coeff[0]= propertiesbarrier[2]-propertiesQW[2] //Band discontinuety or
confinment potential of conduction band using model-solid theory
coeff[1]=propertiesQW[3] //electron mass in conduction band of QW
coeff[2]=propertiesbarrier[3] //electron mass in conduction band of
barrier
coeff[3]=thickness

if( ParamIsDefault(q))
printf "Potential: %g\r",coeff[0]
printf "Carrier mass QW: %g\r", coeff[1]
printf "Carrier mass barrier: %g\r", coeff[2]
endif

//FindRoots /L=0 /H=(0.10) /Q Symteric_finiteQW, coeff

lower=(pi*PlanckConstantReduced)^2/((coeff[3]*1e-
9)^2*2*coeff[1]*electronmass*eVtoJoul)-coeff[0] // Looking for the extrma
in the tan fkt. We have to restrict search to the lower part before the
first extrema
if (lower>0)
lower=-0.000001
endif

FindRoots /L=(-coeff[0]) /H=(lower) /Q semifinite_QW, coeff //Finding the
zeos - care has to be taking tofind the first state and not the excited
states.

if (V_flag !=0)
printf "Problems with Elc at thickness: %g\r", coeff[3]
printf "Error: %g\r", V_flag
endif

Elc=V_root // Energy state in conduction band

//Redo the same for the valence bands and the holes inside

coeff[0]=0.43*(propertiesbarrier[0]-propertiesQW[0]) //Band discontinuety
or confinment potential of conduction band
//coeff[0]=propertiesQW[1]-propertiesbarrier[1]
coeff[1]=propertiesQW[4] //hole mass in valenceband of QW
coeff[2]=propertiesbarrier[4] //hole mass in valenceband of barrier

if( ParamIsDefault(q))
printf "Potential: %g\r",coeff[0]
printf "Carrier mass QW: %g\r", coeff[1]
printf "Carrier mass barrier: %g\r", coeff[2]
endif

//FindRoots /L=0 /H=(coeff[0]/coeff[3]) /Q /T=1e-20 Symteric_finiteQW,
coeff

lower=(pi*PlanckConstantReduced)^2/((coeff[3]*1e-
9)^2*2*coeff[1]*electronmass*eVtoJoul)-coeff[0]

if (lower>0)
lower=-0.000001
endif

FindRoots /L=(-coeff[0]) /H=(lower) /Q semifinite_QW, coeff

```

```

if (V_flag !=0)
printf "Problems with Elv at thickness: %g\r", coeff[3]
printf "Error: %g\r", V_flag
endif

Elv=V_root

// Define the transition energy as barrier band gap plus the two
negatibve energies found for valence and conduction band.

V0=propertiesbarrier[0]+Elc+Elv

if( ParamIsDefault(q))
printf "Energy Conductionband: %g\r", Elc
printf "Energy Valenzband: %g\r", Elv
printf "Transitionenergy: %g\r", V0
endif

killwaves propertiesQW,propertiesbarrier,coeff

if (q==1)
return V0
elseif (q==2)
return Elc
elseif (q==3)
return Elv
else
return V0
endif

End

Function AlGaAs_QW_transition(al_content,thickness,[q])

//Calcualtes the transition energy in an unstrained AlGaAs/GaAs Qw
assuming finite barrieres of infinite thickness and a QW thickness
//
//Fuinction follows Suwits Mathematica sheet
//
//Version 1.0 27.01.2017
//
//returns transition energie and needs Al content of Barrier and GaAs
thickness as input
//
// Eq. for QW can be found inS. Adachi, GaAs and Related Materials, World
Scientific
// The given solution is wrong after Suwit and Wikipedia
//

Variable al_content,thickness,q

Variable V0, Elc,Elv, lower

Make/D /N=10 propertiesQW,propertiesbarrier,coeff

AlGaAs_prop(0,propertiesQW,q=1)
AlGaAs_prop(al_content,propertiesbarrier,q=1)

//calculate energy state of the vallence band

```

```

coeff[0]=0.57*(propertiesbarrier[0]-propertiesQW[0]) //Band discontinuety
or confinement potential of conduction band using band gap and band
offset ratios (ca. 0.5) from literature
//coeff[0]= propertiesbarrier[2]-propertiesQW[2] //Band discontinuety or
confinement potential of conduction band using model-solid theory
coeff[1]=propertiesQW[3] //electron mass in conduction band of QW
coeff[2]=propertiesbarrier[3] //electron mass in conduction band of
barrier
coeff[3]=thickness

if( ParamIsDefault(q))
printf "Potential: %g\r",coeff[0]
printf "Carrier mass QW: %g\r", coeff[1]
printf "Carrier mass barrier: %g\r", coeff[2]
endif

//FindRoots /L=0 /H=(0.10) /Q Symteric_finiteQW, coeff

lower=((pi*PlanckConstantReduced)/(coeff[3]*1e-
9*sqrt(2*coeff[1]*electronmass*eVtoJoul)))^2-coeff[0] // Locing for the
extrma in the tan fkt. We have to restrict search to the lower part
before the first extrema
if (lower>-0.1)
lower=0
endif

FindRoots /L=(-coeff[0]) /H=(lower) /Q Symteric_finiteQW, coeff //Finding
the zeos - care has to be taking tofind the first state and not the
excited states.

if (V_flag !=0)
printf "Problems with Elc at thickness: %g\r", coeff[3]
printf "Error: %g\r", V_flag
endif

Elc=V_root // Energy state in conduction band

//Redo the same for the valence bands and the holes inside

coeff[0]=0.43*(propertiesbarrier[0]-propertiesQW[0]) //Band discontinuety
or confinement potential of conduction band
//coeff[0]=propertiesQW[1]-propertiesbarrier[1]
coeff[1]=propertiesQW[4] //hole mass in valenceband of QW
coeff[2]=propertiesbarrier[4] //hole mass in valenceband of barrier

if( ParamIsDefault(q))
printf "Potential: %g\r",coeff[0]
printf "Carrier mass QW: %g\r", coeff[1]
printf "Carrier mass barrier: %g\r", coeff[2]
endif

//FindRoots /L=0 /H=(coeff[0]/coeff[3]) /Q /T=1e-20 Symteric_finiteQW,
coeff

lower=((pi*PlanckConstantReduced)/(coeff[3]*1e-
9*sqrt(2*coeff[1]*electronmass*eVtoJoul)))^2-coeff[0]

if (lower>-0.1)
lower=0

```

```

endif

FindRoots /L=(-coeff[0]) /H=(lower) /Q Symteric_finiteQW, coeff

if (V_flag !=0)
printf "Problems with Elv at thickness: %g\r", coeff[3]
printf "Error: %g\r", V_flag
endif

Elv=V_root

// Define the transition energy as barrier band gap plus the two
negatibve energies found for valence and conduction band.

V0=propertiesbarrier[0]+Elc+Elv

if( ParamIsDefault(q))
printf "Energy Conductionband: %g\r", Elc
printf "Energy Valenzband: %g\r", Elv
printf "Transitionenergy: %g\r", V0
endif

killwaves propertiesQW,propertiesbarrier,coeff

if (q==1)
return V0
elseif (q==2)
return Elc
elseif (q==3)
return Elv
else
return V0
endif

End

//-----
-----
-----

Function Plot_value(Al_content,In_content,Property)

// Returns a material property value for a given set of parameters.
Practical, if you need
// to know some specific parameter or want to plot it. Also usefull, if
you need to calculate strain
// for any substrate

Variable Al_content,In_content,Property

Wave properties
Variable value

Make /N=10 properties

InAlGaAs_prop(In_content,Al_content,1,properties,q=1)

value=properties[Property]

```

```
killwaves properties
```

```
return value
```

```
End
```

APPENDIX – II – Used code for band gap and electron wavefunction

```

# 1D sample for solving quantum-poisson

#Begin NextnanoWizard parameter section
$BIAS =0          # Gate voltage(V)
$CAP = 2          # Thickness cap
$ALLOY = 0.3      # Al content of AlGaAs layer
$SIZE = 20        # size of AlGaAs layer (nm)
$DOT = 20         # Quantum dot depth
$Dot_top = 290    # Top width
$Dot_bottom = 120 # Bottom width
$DOPECONC = 3.0e14 # donor concentration of 10nm doping layer (cm^-3)
$DOPEPOS = 65     # distance between AlGaAs-GaAs interface and delta
doping position (nm)
$MINGRID = 0.1    # minimum grid spacing (nm)
$NUMEV = 20       # number of eigenvalues to be calculated
$BARRIER = 0.7   # height of left Schottky barrier (eV)
#End NextnanoWizard parameter section

global{
  simulate2D{

    temperature = 300

    substrate{ name = "GaAs" }

    crystal_zb{
      x_hkl = [0, 0, 1]
      y_hkl = [1, 1, 0]
    }
  }<>

  grid{
    xgrid{
      line{ pos = 0          spacing = 0.1 } #cap
      line{ pos = $CAP       spacing = 0.1 } #begin AlGaAs
      line{ pos = $CAP+$DOT  spacing = 0.1 }
      line{ pos = $CAP+$SIZE spacing = 0.1 } #end AlGaAs and
2DEG
      line{ pos = $CAP+$DOT+$SIZE spacing = 0.1 }
      line{ pos = 400        spacing = 5 } #after baggate
    }
    ygrid{
      line{ pos = 0          spacing = 5 }
      line{ pos = 500-$SIZE-($Dot_top) spacing = 5 }
      line{ pos = 500-$SIZE-($Dot_top/2) spacing = 1 } #left end of
barrier
      line{ pos = 500-$SIZE          spacing = 1 } #Dot left
      line{ pos = 500+$SIZE          spacing = 1 } #Dot right
      line{ pos = 500+$SIZE+($Dot_top/2) spacing = 1 } #Right beginning of
barrier
      line{ pos = 500+$SIZE+($Dot_top) spacing = 5 }
      line{ pos = 1000        spacing = 5.0 }
    }

    periodic{

```

```

        x = no
        y = no
    }
}<>

impurities{
    acceptor{ name = "C" energy = 0.027 degeneracy = 4 } # fully ionized
}<>

# Defines a pinned GaAs cap to 0.7 eV
contacts{
    schottky{
        name = "gate"
        bias = 0
        barrier = $BARRIER
    }

    fermi{
        name = "backgate"
        bias = -$BIAS
    }
}<>

structure{
    output_material_index{}
    output_contact_index{}
    output_impurities{}

    # AlGaAs layer
    region{
        everywhere{} # default material
        ternary_constant{ name = "Al(x)Ga(1-x)As" alloy_x = $ALLOY }
    }

    # GaAs cap layer
    region{
        rectangle{ x = [0, $CAP] y=[0,1000]}
        binary{ name = "GaAs" }
    }

    # doping layer
    region{
        rectangle{ x= [1,395] y=[0,1000] }
        doping{ constant{ name = "C" conc = $DOPECONC } }
    }

    # GaAs substrate
    region{
        rectangle{ x = [$CAP+$SIZE+$DOT, 400] y=[0,1000]}
        binary{ name = "GaAs" }
    }

    #GaAs dot

    # region{
    #     rectangle{ x = [$CAP, $CAP+$DOT] y=[200,300]}
    #     binary{ name = "GaAs" }
    # }

```

```

# }

region{
  trapezoid{
    # 2D object e.g. a simple
    trapezoid along the x axis
    base_x = [ $CAP, $CAP] # base line extends in x
    direction from 5 to 15 nm
    base_y = [500-($Dot_top/2), 500+($Dot_top/2)] # base
    line has a constant y coordinate y = 25 nm
    top_x = [ $CAP+$DOT, $CAP+$DOT] # top line extends in
    x direction from 8 to 12 nm
    top_y = [500-($Dot_bottom/2), 500+($Dot_bottom/2)] #
    top line has a constant y coordinate y = 30 nm
  }
  binary{ name = "GaAs" }
}

# region{
#   rectangle{ x = [$CAP+$DOT, $CAP+$DOT+$SIZE] y=[0,200-$SIZE]}
#   binary{ name = "GaAs" }
# }

region{
  trapezoid{
    # 2D object e.g. a simple
    trapezoid along the x axis
    base_x = [ $CAP+$DOT, $CAP+$DOT] # base line extends
    in x direction from 5 to 15 nm
    base_y = [0, 500-($Dot_top/2)-$SIZE] # base line has a
    constant y coordinate y = 25 nm
    top_x = [ $CAP+$DOT+$SIZE, $CAP+$DOT+$SIZE] # top
    line extends in x direction from 8 to 12 nm
    top_y = [0, 500-($Dot_bottom/2)-$SIZE] # top line has
    a constant y coordinate y = 30 nm
  }
  binary{ name = "GaAs" }
}

# region{
#   rectangle{ x = [$CAP+$DOT, $CAP+$DOT+$SIZE] y=[300+$SIZE, 500]}
#   binary{ name = "GaAs" }
# }

region{
  trapezoid{
    # 2D object e.g. a simple
    trapezoid along the x axis
    base_x = [ $CAP+$DOT, $CAP+$DOT] # base line extends
    in x direction from 5 to 15 nm
    base_y = [500+($Dot_top/2)+$SIZE, 1000] # base line has
    a constant y coordinate y = 25 nm
    top_x = [ $CAP+$DOT+$SIZE, $CAP+$DOT+$SIZE] # top
    line extends in x direction from 8 to 12 nm
    top_y = [500+($Dot_bottom/2)+$SIZE, 1000] # top line
    has a constant y coordinate y = 30 nm
  }
  binary{ name = "GaAs" }
}

# Top gate (Schottky contact)
region{
  rectangle{ x = [0, 1] y=[0,1000]}
}

```

```

    contact{ name = "gate" }
}

# Back gate (Ohmic contact)
region{
  rectangle{ x = [390, 400] y=[0,1000]}
  contact{ name = "backgate" }
}
}<>

classical{
  Gamma{}
  L{}
  X{}
  HH{}
  LH{}
  SO{}

  output_bandedges{averaged = no}
  output_carrier_densities{}
  output_ionized_dopant_densities{}
  output_intrinsic_density{}
  output_bandgap{}
}<>

quantum {
  region{
    name = "DOT"
    x = [0, 100] y=[500- $\text{\$Dot\_top}$ ,500+ $\text{\$Dot\_top}$ ]
    Gamma{ num_ev =  $\text{\$NUMEV}$  }
    HH { num_ev =  $\text{\$NUMEV}$  }
    LH { num_ev =  $\text{\$NUMEV}$  }
    output_wavefunctions{ probabilities = no max_num =  $\text{\$NUMEV}$  }
  }
}<>

poisson{
  newton_solver{ residual = 1e-9 }
  output_potential{}
  output_electric_field{}
}<>

currents{
  insulator_bandgap = 1
  output_fermi_levels{}
}<>

output{

  # format2D = Origin
  section1D{ # output a 1D section of the simulation
area (1D slice)
  name = "x1" # name of section enters file name

  y = 500-( $\text{\$Dot\_top}$ /2) # 1D slice at y = 100 nm

```

```

}

section1D{                                # output a 1D section of the simulation
area (1D slice)
  name = "x2"                              # name of section enters file name

  y = 500.0                                # 1D slice at y = 100 nm

}
section{  name      = "zoom"
  range_x = [0,100]          # x = [0, 100] y=[500-
$Dot_top,500+$Dot_top]
  range_y = [500-$Dot_top,500+$Dot_top] }
}<>

run{
  solve_poisson{}
  solve_quantum{}
  outer_iteration{} # solve coupled Schrödinger-Poisson equations
}<>

```